11-13-2020

Plio-Pleistocene Antarctic Ice-Ocean Interactions in the Ross Sea

Catherine Prunella
University of South Florida

Plio-Pleistocene Antarctic Ice-Ocean Interactions in the Ross Sea

by

Catherine Prunella

A thesis submitted in partial fulfillment
of the requirements for the degree of
Master of Science in Marine Science
with a concentration in Geological Oceanography
College of Marine Science
University of South Florida

Major Professor: Amelia E. Shevenell, Ph.D.
Tim M. Conway, Ph.D.
Robert M. McKay, Ph.D.

Date of Approval:
November 13, 2020

Keywords: Paleoclimate, foraminifers, geochemistry, Mg/Ca, stable isotopes

Acknowledgments

This International Ocean Discovery Program (IODP)-based research was funded by a United States Science Support Program (USSSP) post-expedition award to Dr. Amelia Shevenell. Salary support was provided by University of South Florida College of Marine Science internal fellowships awarded to me, Catherine Prunella, including: the Anne and Werner von Rosenstiel Endowed Fellowship, the Jack and Katharine Ann Lake Fellowship in Marine Science, and the Thomas E. Pyle Memorial Fellowship in Marine Science. This research uses sediment cores collected on IODP Expedition 374 to the Ross Sea. We thank the Expedition 374 shipboard scientific party, support staff, and crew of the D/V *JOIDES Resolution* for recovering, analyzing, and curating the sediment cores used in my research.

I thank my research advisor Dr. Amelia Shevenell for providing an ambitious and exciting research project, and for her financial, professional, and emotional support. I thank Dr. Tim Conway and Dr. Robert McKay (UVictoria, Wellington) for serving on my committee and providing insightful comments. I thank Ethan Goddard for helping me analyze hundreds of Site U1523 samples for stable isotopes, supporting the Mg/Ca method development, and for his enthusiasm and patience as a teacher. I thank Dr. Denise Kulhanek (TAMU) for working with me to develop the Site U1523 composite depth scale, Dr Sunghan Kim (KOPRI) for assistance with developing the Site U1523 age model, and Benjamin Griffin (UVictoria) for his detailed lithologic descriptions and grain size analyses. I thank Michelle Guitard, Kara Vadman, and Imogen Browne for their scientific insights and friendship, with a nod to Kara Vadman for

assistance with cleaning Site U1523 foraminifers for Major and Trace Element/Calcium analyses.

To Mark, thank you for helping me stay grounded and fed, even after working 12-hour night shifts. To my family, thank you for your lifelong love, support, and encouragement. I became infatuated with Earth Science somewhere between the rocky shores of Wading River and the willow tree in the Bronx Botanical Gardens. Thank you for helping me get tangled up in the blue of this world.

Table of contents

List of tables iii

List of figures iv

Abstract v

Contribution statement 1

1 Introduction 3
- 1.1 The role of ocean heat on Antarctica's ice sheets 3
- 1.2 Cenozoic climate and ice sheet evolution 4
- 1.3 Unravelling northern and southern hemispheric ice volume signals during the Plio-Pleistocene 7
  - 1.3.1 Antarctic continental margin records 7
- 1.4 Overarching goal of research, approach, hypothesis testing 8
  - 1.4.1 Hypothesis and scientific goal 8
  - 1.4.2 Approach 9

2 Study setting 12
- 2.1 Site U1523 location and physical oceanography 12
- 2.2 $\delta^{13}C$ as a proxy for productivity and water mass presence 14
- 2.3 Lithostratigraphy and depositional environment 14

3 Materials and methods 16
- 3.1 Foraminifer sampling and preparation for geochemical analyses 16
- 3.2 Foraminifer stable isotope analyses 16
- 3.3 Trace element/Calcium preparation and analyses 17
  - 3.3.1 Foraminifer cleaning 17
  - 3.3.2 Blank and standard preparation 18
  - 3.3.3 Instrumentation 19
  - 3.3.4 Data processing 20
  - 3.3.5 Matrix effects 22

4 Composite depth scale 24

5 Chronology 25
- 5.1 Shipboard chronology 25
- 5.2 Shorebased chronology 25

6 Results 30

6.1 Foraminifer stable isotopes 30
6.1.1 Oxygen Isotopes ($\delta^{18}O$) 30
6.1.2 Carbon isotopes ($\delta^{13}C$) 32
6.2 $\delta^{18}O$, $\delta^{13}C$, and MS records from 0-25 m CCSF 33
6.3 Foraminifer Mg/Ca 35
6.3.1 Monitoring Mg/Ca contaminants 35
6.3.2 Mg/Ca in the top 25 m CCSF 37

7 Discussion 39
7.1 Fidelity of stable isotopes and Mg/Ca measurements 39
7.1.1 Mg/Ca-temperature calculations 39
7.1.2 Dissolution and diagenetic influence 41
7.1.3 Mg/Ca secondary influences 43
7.2 Long-term Plio-Pleistocene Ross Sea temperature and ice volume changes 44
7.3 Late Pleistocene mCDW presence on the Ross outer shelf 48

8 Conclusions 50

References 51

Appendix A: Extended data 64

Appendix B: Permissions 70

List of tables

Table 1: Measures of accuracy and precision in Mg/Ca reference materials 22

Table 2: U1523 age control points.....28

Extended data table 1A: Elemental concentrations in standard solutions 64

Extended data table 2A: Stratigraphic splice used for the U1523 composite depth scale (CCSF).....65

List of figures

Figure 1: Satellite measurements of Antarctic mass loss (red circles) and gain (blue circles) from 1979-2017 and ocean temperatures at 310 meters depth.....4

Figure 2. Cenozoic composite benthic foraminifer $\delta^{18}O$ record.....6

Figure 3: IODP Site U1523 location and oceanography 13

Figure 4: Calcium matrix effects on Mg/Ca in standards and samples 23

Figure 5: Lithology and chronology in the U1523 Plio-Pleistocene sequence.....26

Figure 6: Revised mid-late Pleistocene chronology in the top 16 m CCSF 27

Figure 7: Foraminifer $\delta^{18}O$ and $\delta^{13}C$ from U1523 spanning the Plio-Pleistocene 31

Figure 8: High-resolution MS and isotopes in the top 25 m CCSF (1.9-0 Ma) of U1523 35

Figure 9: Linear correlations between Mg/Ca, Mn/Ca and Fe/Ca in foraminifers 36

Figure 10: MS, Mg/Ca, and $\delta^{18}O$ in the top 25 m CCSF (1.9-0 Ma) 38

Figure 11: Mg/Ca-temperatures spanning the last 1.4 Ma.....40

Figure 12: Antarctica's contribution to the global ice volume record over the last 3.2 Ma 45

Figure 13: Paleoceanographic changes in the Ross Sea during the mid-late Pleistocene 47

Extended data figure 1A: Typical XR ICP-MS sequence for trace element/Ca analysis.....66

Extended data figure 2A: U1523 detailed lithology, physical properties, and XRF-Zr/Rb records used to generate the splice.....67

Extended data figure 3A: Rescaled physical properties and Zr/Rb against the composite depth below sea floor (CCSF) scale 69

Abstract

Warm, intermediate-depth Southern Ocean waters are implicated in recent Antarctic ice mass loss. Direct observations of Antarctic Ice Sheet (AIS) retreat are temporally limited, necessitating paleoceanographic records of ocean-ice interactions during past warm climate intervals. Deep-sea and ice-proximal sediments record orbitally-paced glacial-interglacial fluctuations in AIS volume during the Plio-Pleistocene (last 5 million years; Ma), but the total contribution of the AIS and the role of ocean heat in these fluctuations remain unresolved. To address the response of Antarctica's ice sheets to changing ocean temperatures during the Plio-Pleistocene, International Ocean Discovery Program (IODP) Expedition 374 recovered sediments from the Ross Sea outer-shelf at Site U1523. Site U1523 is close to the shelf break and sensitive to incursions of warm intermediate-depth Southern Ocean waters. Site U1523 sediments include foraminifer-bearing/rich sands and muds, which enable development of benthic (*Trifarina* sp.) and planktic (*N. pachyderma* sinistral) foraminifer stable oxygen ($\delta^{18}O$) and carbon ($\delta^{13}C$) isotope records. Here we present foraminifer $\delta^{18}O$, $\delta^{13}C$, and Mg/Ca records from the upper 90 m of U1523, which spans the late Pliocene to Holocene (last 3.1 Ma). We provide a new chronology for the U1523 Pleistocene sedimentary sequence by correlating diatom-bearing muds with low magnetic susceptibility (MS) to interglacial periods of the last 0.65 Ma. Benthic and planktic foraminifer $\delta^{18}O$ values increase by ~1.5‰ up-section, which reflects long-term global cooling and ice growth, with orbital-scale ice volume and temperature variability superimposed. Our isotope records include an abrupt shift at 16 m CCSF, which we interpret as a hiatus due to an increase in ice-volume and bottom water production during the mid-Pleistocene transition. To

separate the ice volume and temperature signals contained in the $\delta^{18}O$ signal, we analyzed Mg/Ca in benthic and planktic foraminifers. Our Mg/Ca records reveal a 4.4°C and 4.8°C cooling in deep and surface waters, respectively, over the last 3.1 Ma, consistent with Plio-Pleistocene cooling estimated from deep sea Mg/Ca records. This is the first application of Mg/Ca paleothermometry in ice-proximal sediment for the Plio-Pleistocene, and although temperature reconstructions are high, Mg/Ca fluctuations parallel changes in sedimentology, $\delta^{18}O$, and $\delta^{13}C$, suggesting retainment of a primary environmental signal. Pleistocene surface water estimates are up to 11°C high, and exhibit a distinct decrease at ~0.40 Ma to values similar to modern. Warm perturbations in bottom water temperatures of 4-5°C are synchronous with lithologic transitions at depths that may correlate to MIS 31, 13 and 10 through 5. These warm spikes coincide with low $\delta^{13}C$ and planktic $\delta^{18}O$, and shifts in MS, suggesting a mechanistic link between warm ocean temperatures, meltwater input, and ocean circulation. These records provide the first ice-proximal evidence of paired ocean temperature and ice volume fluctuations during the mid-late Pleistocene. We interpret the relationship between low $\delta^{13}C$ and high Mg/Ca to reflect intervals of stronger modified Circumpolar Deep-Water presence on the Ross Shelf, that may be responsible for ice loss suggested by low $\delta^{18}O$. Despite assumptions regarding ocean temperatures and the $\delta^{18}O$ of glacial ice, our $\delta^{18}O_{sw}$ records demonstrate ~100 Kyr cyclicity in ice sheet fluctuations following the mid Pleistocene Transition, consistent with deep-sea records of eccentricity-paced climate oscillations. We conclude that Ross Sea circulation and temperature changes coincide with ice volume fluctuations during the mid-late Pleistocene, though improvements in the U1523 chronology are necessary to confirm the exact timing of ice-ocean interactions.

Contribution statement

This research involves sediment cores collected during the IODP Expedition 374 to the Ross Sea, Antarctica. Planning for Expedition 374 began nearly a decade ago, and culminated in the 2018 Expedition led by Co-Chief Scientists Dr. Robert McKay, Dr. Laura DeSantis, and Project Manager/Staff Scientist Dr. Denise Kulhanek. This Master's thesis addresses one of the primary scientific objectives of Expedition 374: to assess the role of oceanic forcing on Antarctic Ice Sheet stability (McKay et al., 2019). To do so, I (Catherine Prunella) generated stable isotope and trace element ratios (TE/Ca) in foraminifers spanning the Plio-Pleistocene sedimentary sequence of Site U1523. My advisor, Dr. Amelia Shevenell, was a proponent of the Expedition 374 proposal and conceptualized the Master's research. I picked planktic and benthic foraminifers in over 400 samples, prepared samples for geochemical analysis, and together with lab manager Ethan Goddard, measured samples for stable isotopes. With Ethan Goddard, I developed a method for measuring TE/Ca in foraminifers on the USF-CMS Element XR inductively coupled plasma mass spectrometer, analyzed all samples, and processed all datasets. My additional contributions to U1523 include: scanning sediment cores for X-ray fluorescence at the IODP Gulf Coast Repository at Texas A&M University; assisting Dr. Kulhanek in generating the composite depth scale; and generating a new chronology in the top 20 m. My geochemical data and interpretations provide knowledge on oceanographic and ice evolution in the Ross Sea over the Plio-Pleistocene. This information will be incorporated into ongoing and future research by the Expedition 374 team, including (but not limited to) studies of Ross Sea foraminiferal

assemblages, seismic and sequence stratigraphy, sediment provenance, and modeling of ice-ocean interactions.

1 Introduction

1.1 The role of ocean heat on Antarctica's ice sheets: Over the past 40 years, satellite observations document thinning and retreat of Antarctica's marine-terminating glaciers and their buttressing ice shelves (Shepherd et al., 2004; Rignot et al., 2013; Rye et al., 2014; Rignot et al., 2019) (Figure 1). Between 2003 and 2019, ice loss from Antarctica contributed 5.2 mm of sea level equivalent from 2003-2019 (Smith et al., 2020), and ice sheet models predict increasing Antarctic ice mass loss with the potential to contribute up to ~1 m to global sea level rise by 2100 (Golledge et al., 2015; DeConto and Pollard. 2016). Presently, ice mass loss is often associated with Circumpolar Deep Water (CDW), a warm (>1^{o}C), nutrient-rich intermediate-depth water mass that upwells on to Antarctica's continental shelves and accesses glacial grounding lines (Rignot and Jacobs, 2002; Pritchard et al., 2012; Cook et al., 2016; Shepherd et al., 2018; Gudmundsson et al., 2019). CDW-derived heat over Antarctica's continental shelves increases basal melt rates of ice shelves and glacial grounding line retreat, which threatens the stability of Antarctica's marine terminating ice (Rignot and Jacobs, 2002; DeConto and Pollard, 2016; Shepherd et al., 2018). Over the last four decades, CDW has warmed (~0.1°C per decade) and the frequency of upwelling events may have increased (Schmidtko et al., 2014; Marshall, 2003; Thompson and Solomon, 2002; Thoma et al., 2008; King et al., 2018).

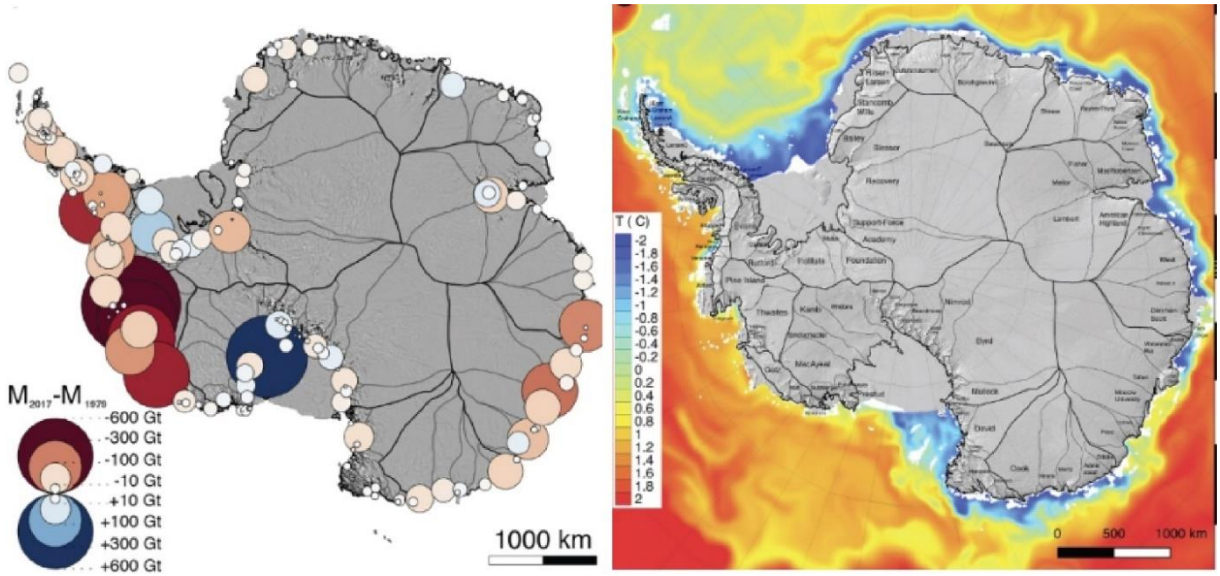

Figure 1. Satellite measurements of Antarctic mass loss (red circles) and gain (blue circles) from 1979-2017 and ocean temperatures at 310 meters depth. Modified from "Four decades of Antarctic Ice Sheet mass balance from 1979–2017," by Rignot et al. (2019), Proceedings of the National Academy of Sciences, 116 (4), 1095–1103.

Ice-proximal Southern Ocean temperature observations are limited to the last 50 years, and are confined to easily accessible regions (Rignot et al., 2019). Longer-term records of ocean-ice interactions can be reconstructed from ice-proximal marine sediments. These records are essential for constraining the role of ocean temperature on past ice retreat (Escutia et al., 2019). However, few proxy-based ocean temperature reconstructions exist from Antarctica's continental margin sediments (Whitehead and Bohaty, 2003; Escutia et al., 2009; Shevenell et al., 2011; McKay et al., 2012a; Beltran et al., 2020), limiting understanding of ocean-ice interactions over the last 5 million years (Ma).

1.2 Cenozoic climate and ice sheet evolution: Deep-sea benthic foraminifer stable oxygen isotopes ($\delta^{18}O$) provide insight into Antarctica's ice sheet history and temperatures over the last 65 million years (Shackleton and Kennett, 1975; Zachos et al., 2001; Miller et al., 1991; Cramer et al., 2009; Westerhold et al., 2020) (Figure 2). Foraminifer $\delta^{18}O$ is a function of ocean temperature and the $\delta^{18}O$ of seawater ($\delta^{18}O_{sw}$), and the latter is influenced by global ice volume

and local freshwater input. Benthic $\delta^{18}O$ indicates step-wise growth of Antarctica's cryosphere at the Eocene-Oligocene boundary (~34 Ma) and middle Miocene Climate Transition (14.2-13.8 Ma), each culminating in a ~1.0‰ increase in benthic $\delta^{18}O$ records (Kennett, 1977; Coxall et al., 2005; Shackleton and Kennett, 1975; Flower and Kennett 1994). However, after the onset of Northern Hemisphere glaciation at 2.7 Ma (Shackleton et al., 1984; Haug and Tiedemann, 1998; Ravelo et al., 2004), benthic foraminifer $\delta^{18}O$ records cannot be used to differentiate between Northern and Southern Hemisphere ice growth because $\delta^{18}O$ is a function of global ice volume and ocean temperature. Pliocene and Pleistocene (Plio-Pleistocene) ice sheet fluctuations are orbitally-paced, and switch from 41 thousand year (Kyr) to 100 Kyr pacing at the middle Pleistocene Transition (MPT; 1.2-0.6 Ma; Lisiecki and Raymo 2005). Composite benthic $\delta^{18}O$ records reveal pronounced interglacial conditions during several Pleistocene Marine Isotope Stages (e.g. MIS 31, 11, 5; Lisiecki and Raymo 2005); however, the magnitude of Antarctic ice mass loss during these "super-interglacials" is obscured in the $\delta^{18}O$ signal, due to the convoluting influences of bipolar glaciation and global cooling on far-field $\delta^{18}O$ records.

Foraminifer magnesium to calcium (Mg/Ca) is a standard deep-sea paleothermometer that can be measured on the same foraminifer calcium carbonate ($CaCO_3$) as $\delta^{18}O$ to provide information on global ice volume and the interactions between oceanic heat and marine-terminating ice, because Mg/Ca-based temperatures allow us to deconvolve global ice volume and temperature in $\delta^{18}O$ records (Mashiotta et al., 1999; Lear et al., 2000; Billups and Schrag, 2002; Shevenell et al., 2004). Paired $\delta^{18}O$ and Mg/Ca records reveal ocean cooling accompanied ice growth at the Eocene-Oligocene (Bohaty et al., 2012), middle Miocene (Shevenell et al., 2004; Shevenell et al., 2008), and Plio-Pleistocene (Billups and Schrag, 2002) transitions. Mg/Ca records document deep-sea cooling of ~12 ^{o}C throughout the Cenozoic (Lear et al., 2000), and

4°C at the Plio-Pleistocene transition (Lear et al., 2000; Billups and Schrag, 2002). Despite its utility, Mg/Ca paleothermometry has never been employed in Antarctic margin sediments over the Plio-Pleistocene due to a lack of $CaCO_3$ in Antarctic coastal sediment and issues with the cold end of Mg/Ca-temperature calibrations. The present-day $CaCO_3$ saturation state in the Southern Ocean is low compared to other major ocean basins due to high CO_2 solubility in cold and saline waters, and high primary productivity (Feely et al., 2009; DeJong et al., 2015; Kennett, 1966). In the Ross Sea, the calcium compensation depth is estimated to be shallow (350–550 meters; Fillon, 1974; Kennett, 1966) and exhibits regional variability related to productivity, water mass presence, and topography (Osterman and Kellogg, 1979; Prothro et al., 2018). Recovery of foraminifers in Antarctic shelf sediments are rare, and where present are limited to specific regions where oceanographic, biologic, and sedimentologic conditions facilitate $CaCO_3$ preservation.

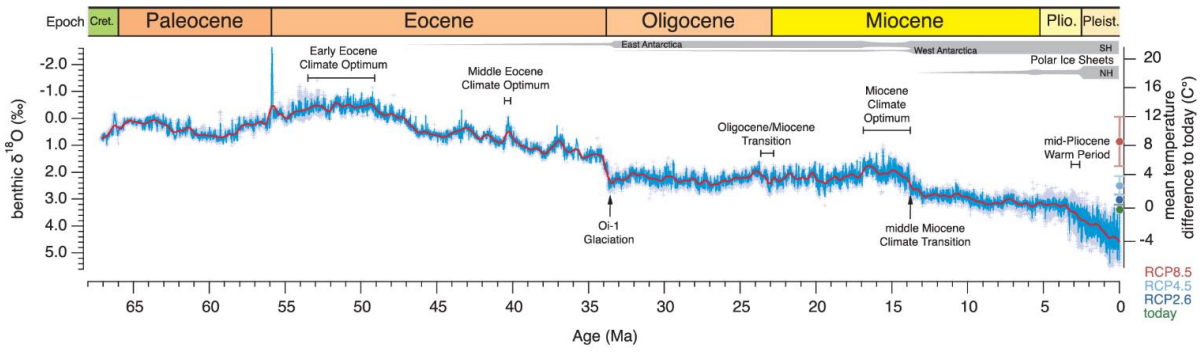

Figure 2. Cenozoic composite benthic foraminifer $\delta^{18}O$ record. The timing of major climate transitions and ice growth in the Southern (SH) and Northern Hemisphere (NH) are labeled. Modified from "An astronomically dated record of Earth's climate and its predictability over the last 66 million years" by Westerhold et al. (2020). Science, 369 (6509), 1383-1387.

1.3 Unravelling northern and southern hemispheric ice volume signals during the Plio-Pleistocene

1.3.1 Antarctic continental margin records: Ice-proximal sediment records are essential for assessing the source of global ice volume captured in Pleistocene $\delta^{18}O$ fluctuations. Marine sediments from Antarctica's continental margins provide direct physical evidence of Antarctic ice sheet behavior during the Plio-Pleistocene through seismic (Alonso et al., 1992), lithofacies (Naish et al., 2009; McKay et al., 2012b), ice rafted debris (Patterson et al., 2014), and provenance data (Cook et al., 2013; Bertram et al., 2018; Wilson et al., 2018). These ice-proximal records reveal the retreat of Antarctica's marine terminating outlet glaciers during warm climate conditions of the early to middle Pliocene (Naish et al., 2009; Cook et al., 2013; Patterson et al., 2014; Bertram et al., 2018) and some Pleistocene interglacials (e.g., MIS 31, 15-13, 11, 9, 7, and 5e) (Scherer et al., 1998; McKay et al., 2012b; Teitler et al., 2015; Hillenbrand et al., 2009; Wilson et al., 2018; Turney et al., 2020; Blackburn et al., 2020).

Oceanic warming is implicated in modern Antarctic ice sheet mass loss (Pritchard et al., 2012; Rignot et al., 2013; Cook et al., 2016; Shepherd et al., 2018, Rignot et al., 2019), and models paired with Antarctic marine geologic records highlight the importance of relatively warm ice-proximal ocean waters on past and future ice retreat (Deconto and Pollard, 2016; Golledge et al., 2015). Ranges of ocean temperatures estimates from microfossil assemblages in Prydz Bay and Antarctic Peninsula sediment suggest ocean temperatures of >5^{o}C warmer during the mid-late Pliocene (4-3.5 Ma) (Escutia et al., 2009). Marine geologic, geochemical, and micropaleontologic records from the Ross Sea at AND-1B also document relatively warm Ross Sea surface waters during the Pliocene (up to ~10^{o}C), and synchronous cooling and ice growth between 4.5 and 2.0 Ma (McKay et al., 2012a). Diatom (Scherer et al., 2008) and

coccolithophores (Villa et al., 2012) assemblages in the Ross embayment indicate warm surface waters during MIS 31, and a diatomite sedimentary sequence in the AND-1B drill core reveals contemporaneous ice retreat (Naish et al., 2009; McKay et al., 2012b). Organic biomarkers in ice-proximal and Southern Ocean sediment suggest elevated sea surface temperatures during MIS 31 (Beltran et al., 2020), and ice sheet-shelf modelling of MIS 31 suggest a collapse of marine-based sectors of the WAIS, largely driven by oceanic heat and sub-ice-shelf melting (Pollard and DeConto, 2009; DeConto et al., 2012). Antarctic ice core records indicate warmer-than-present atmospheric temperatures during late Pleistocene interglacials (Jouzel et al., 2007), but the role of oceanic heat in driving Antarctic ice loss during late Pleistocene interglacials remains unknown (Wilson et al., 2018).

1.4 Overarching goal of research, approach, hypothesis testing

1.4.1 Hypothesis and scientific goal*: We hypothesize that changes in wind driven currents enhanced heat delivery onto the continental shelf via CDW incursions, which drove ice retreat in the Ross Sea during Plio-Pleistocene warm intervals.* We test this hypothesis with the first high-resolution Plio-Pleistocene (3 Ma to Holocene) planktic (*Neogloboquadrina pachyderma* sinistral) and benthic (*Trifarina* sp.) foraminifer $\delta^{18}O$, $\delta^{13}C$, and Mg/Ca records from coastal Antarctic sediment at International Ocean Discovery Program (IODP) Site U1523 on the outer Ross Sea continental shelf. Site U1523 provides a unique opportunity to study the influence of oceanic heat on Antarctic ice sheet dynamics, because U1523 is close to the Ross Sea shelf break and sensitive to incursions of warm intermediate-depth Southern Ocean waters. *We hypothesize that ambient ocean temperatures are reflected in the Mg/Ca of N. pachyderma and Trifarina.* We convert Mg/Ca to temperature using established calibrations (Elderfield et al., 2010; Vázquez Riveiros et al., 2016) and use temperatures to isolate the ice volume signal from $\delta^{18}O$

(Shackleton, 1974). We compare Mg/Ca to $\delta^{13}C$ to assess changes in ocean circulation on the Ross shelf, and use physical properties of sediment (e.g. magnetic susceptibility) to interpret the depths of glacial and interglacial transitions.

1.4.2 Approach: We compare U1523 lithofacies to foraminifer geochemical records to assess the relationship between ice extent on the Ross continental shelf and oceanographic temperature and circulation. Magnetic Susceptibility (MS) and Natural Gamma Radiation (NGR) are indicators of biogenic and siliciclastic content in sediment, and were analyzed in U1523 sediment during Expedition 374 (McKay et al., 2019). MS is a measure of magnetite minerals which have a terrigenous source, and NGR reflects radioactive isotopes associated with clays (K, U, Th). We use MS and NGR measurements to distinguish between diatom-bearing muds and oozes (low MS/NGR) and sands and diamict sediments (high MS/NGR). Diatom-bearing muds and mudstone in Antarctic margin sediment cores are associated with ice-distal depositional environments conducive to pelagic biosiliceous sedimentation, whereas sands and diamicts are related to ice-proximal depositional processes (Camerlenghi et al., 1997; Hepp et al., 2006; Hillenbrand et al., 2009; Williams et al., 2012; Patterson et al., 2014; Jimenez-Espejo et al., 2020; McKay et al., 2019). Because U1523 is a current-drive site, high MS/NGR also reflects coarse deposits from winnowing bottom currents. MS and NGR records can thus reveal past climate and oceanographic conditions on the Ross shelf.

Foraminifer $\delta^{18}O$ is a function of ocean temperatures, global ice volume, and hydrologic processes. In ice-proximal settings, the $\delta^{18}O_{sw}$ is influenced by isotopically light meteoric waters from glacial meltwater and precipitation (Grobe et al., 1990; Ravelo and Hillaire-Marcel, 2007), which predominantly influence surface waters. We thus use the $\delta^{18}O$ of planktic *N. pachyderma* to assess the meltwater input to the Ross shelf. Advection of water masses may also impact

foraminifer $\delta^{18}O$ in the Ross Sea, because Antarctic water masses carry distinct $\delta^{18}O_{sw}$ signatures (Jacobs et al., 2002).Foraminiferal Mg/Ca can be measured on the same $CaCO_3$ as $\delta^{18}O$ to understand changes in global ice volume (benthics) and meltwater (planktics). However, only one established Mg/Ca record exists from Antarctic margin sediment (Hillenbrand et al., 2017), which is limited to the last 9 Kyr. With abundant foraminifers in recently recovered U1523 sediment cores, we can now generate long-term ice-proximal Mg/Ca paleotemperatures.

While temperature is thought to be the primary factor driving incorporation of Mg into foraminifer $CaCO_3$, secondary factors influence ratios on ocean-wide and local scales. On time scales longer than the residence time of calcium in seawater (1 Ma), secular variations in the Mg/Ca of seawater (Mg/Ca_{sw}) influence the ratio in foraminiferal tests. Reconstructions of Plio-Pleistocene Mg/Ca_{sw} provide evidence for lower whole ocean Mg/Ca_{sw} during the middle Pliocene (~4.4 mmol/mol at 3.2 Ma) than at present (5.2 mmol/mol) (Fantle and DePaolo 2006; Evans et al., 2016). Because foraminifer Mg/Ca and Mg/Ca_{sw} have a positive relationship, if we were to assume constant Mg/Ca_{sw}, Pliocene temperatures would be underestimated. Salinity also exerts a secondary influence on planktic Mg/Ca (Lea et al., 1999; Arbuszewski et al., 2010; Hönisch et al., 2013). On the Ross Sea continental shelf, meltwater released during deglaciation could lower the salinity of surface waters, resulting in lower Mg/Ca and a slight underestimation of ocean temperatures. The carbonate ion concentration ($[CO_3^{2}]$) and saturation state of seawater also exerts secondary influences on foraminiferal Mg/Ca, through dissolution of Mg-rich portions of tests when seawater $[CO_3^{2-}]$ is low (Rosenthal et al., 2006; Elderfield et al., 2006). Changes in seawater, particularly bottom water, $[CO_3^{2-}]$ on glacial-interglacial timescales may bias Mg/Ca-derived temperatures. We expect low $[CO_3^{2-}]$ to relate to lower Mg/Ca-derived

temperatures. Future interpretation of [CO_3^{2-}] indicators, like foraminifer Li/Ca (Lear et al., 2010), will aid our assessment of the [CO_3^{2-}] influence on Mg/Ca.

2 Study setting

2.1 Site U1523 location and physical oceanography: IODP Expedition 374 recovered a total ~134 meters of diatom-rich/bearing mud, ooze, and diamict, and foraminifer-bearing sand, muddy sand, and diamict (for details see 2.3) from Site U1523 spanning the late Miocene to Pleistocene (74°9.02'S 176°47.70′W, 828 m water depth; McKay et al., 2019). U1523 was drilled on the eastern flank of the Iselin Bank, ~18 km south of the Ross Sea shelf break (Figure 3). The site is presently influenced by both on-shelf transport of Circumpolar Deep Water (CDW) and outflow of newly-formed Ross Sea Bottom Water (RSBW) (McKay et al., 2019). Relatively warm, saline, and nutrient-rich CDW originates from the mid-depths of the Antarctic Circumpolar Current and flows poleward into the Ross Gyre (Orsi et al., 1995). CDW upwells onto the Ross Sea shelf and moves south through deep glacially-carved troughs, mixing with Antarctic Surface Water (AASW) to form modified CDW (mCDW), which transports heat to regional marine-terminating grounding lines (Dinniman et al., 2011; Orsi and Wiederwohl, 2009). CDW presence on the Ross Sea continental shelf is modulated by the Antarctic Slope Current (ASC), a vigorous along-slope current modulated by the easterly winds (Gill, 1973; Ainley and Jacobs, 1981; Jacobs, 1991; Thompson et al., 2018). Recent studies indicate that ongoing Antarctic ice mass loss may be associated with a weakening of the ASC, which facilitates warm CDW inflow onto continental shelves (Schmidtko et al., 2014; Thompson et al., 2018). The modern Ross Sea shelf is a cold-water shelf (Schmidtko et al., 2014) due to the regional strength of the ASC, but a thin lens of CDW influences the mid-depths of the Iselin Bank (Site U1523). RSBW, formed from a mixture of dense shelf waters produced within the

Ross Sea polynya southeast of the Iselin Bank (Gill, 1973; Smith et al., 2014) and mCDW, flows northward and cascades downslope through Hilary Canyon (located northeast of Site U1523), ultimately becoming a significant component of Antarctic Bottom Water (AABW) (Carmack, 1977; Orsi et al., 1999; Bergamasco et al., 2002; Gordon et al., 2004; Whitworth and Orsi, 2006; Gordon et al., 2009). Thus, physical oceanographic processes in the Ross Sea contribute substantially to AABW, which ventilates abyssal ocean depths and drives global overturning circulation (Orsi et al., 1999; Dinniman et al., 2011; Morrison et al., 2020).

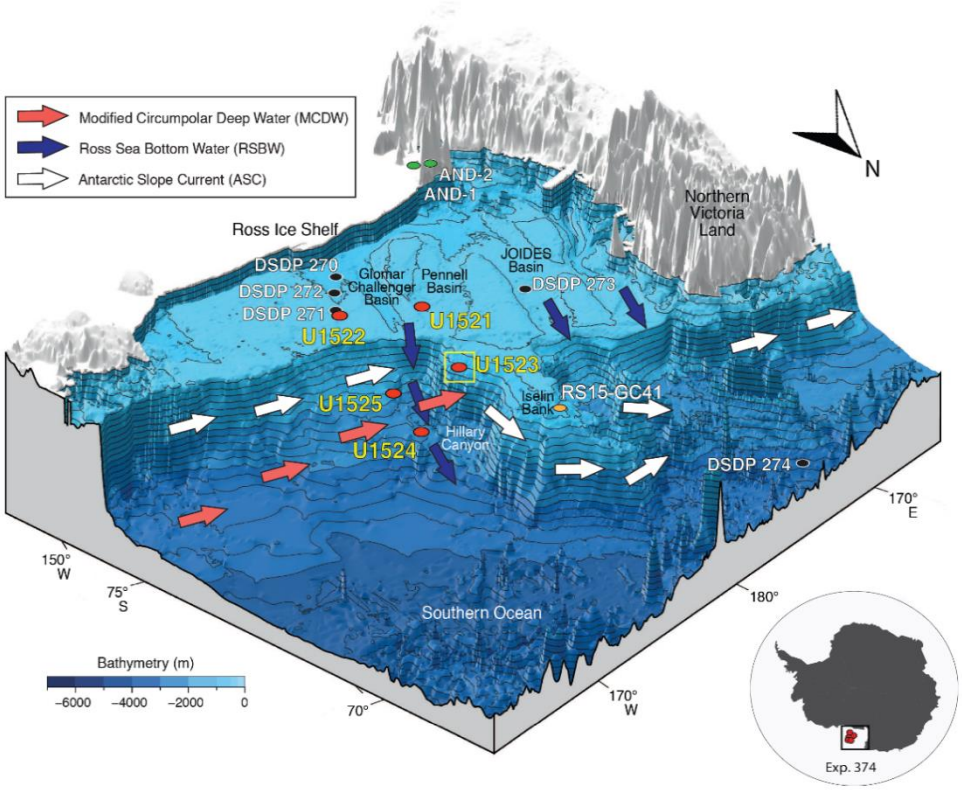

Figure 3: IODP Site U1523 location and oceanography. Site U1523 (yellow box) is located in 828 meters of water on the Iselin Bank at the continental shelf edge of the Ross Sea. IODP (red), DSDP (black), ANDRILL (green) drill sites are indicated. Inset: Antarctica, with Ross Sea Location (black box) and IODP Expedition 374 sites (red). Modified from McKay, R.M., De Santis, L., Kulhanek, D.K., and the Expedition 374 Scientists, 2019. Ross Sea West Antarctic Ice Sheet History. Proceedings of the International Ocean Discovery Program, 374: College Station, TX (International Ocean Discovery Program).

2.2 $\delta^{13}C$ as a proxy for productivity and water mass presence: We use benthic and planktic foraminifer isotopic records to reconstruct water mass influence at Site U1523. Foraminifers incorporate stable carbon isotopes in equilibrium with dissolved inorganic carbon (DIC) in ambient waters, and $\delta^{13}C_{DIC}$ is primarily controlled by local biological cycling of carbon isotopes (^{12}C and ^{13}C) (Kroopnick, 1974; Ravelo and Hillaire-Marcel, 2007; Mackensen and Schmiedl, 2019). Light ^{12}C is preferentially incorporated into organic matter during photosynthesis and released during decay, causing $\delta^{13}C_{DIC}$ enrichment in surface waters and depletion at depth. As water masses age they accumulate respired ^{12}C and gain a depleted $\delta^{13}C$ signature. Foraminiferal $\delta^{13}C$ has been used as a proxy for CDW on Antarctic continental margins because nutrient-rich CDW is depleted in $\delta^{13}C$ relative to Antarctic shelf waters (Shevenell and Kennett, 2002; Hillenbrand et al., 2017). At present-day U1523, benthic foraminifers are under the influence of RSBW, which occupies depths greater than 500 meters (Conte et al., submitted). The planktic species *N. pachyderma* calcifies in the mixed layer and is thought to reproduce below the pycnocline, gaining gametogenic calcite with a geochemical signature reflecting the top 200 meters (Kohfeld et al., 1996; Nyland et al., 2006). At U1523, the modern *N. pachyderma* depth habitat occupies Antarctic Surface Water (AASW) in the top 150 meters and mCDW below (Conte et al., submitted). If foraminifer $\delta^{13}C$ records are primarily influenced by water masses in the Ross Sea, we expect low $\delta^{13}C$ values to reflect intervals of greater mCDW presence.

2.3 Lithostratigraphy and depositional environment: Site U1523 (Holes U1523A, U1523B, and U1523E) was drilled to 170 m core depth below seafloor (CSF-A). Holes A (0-43 core depth below sea floor; CSF-A m) and B (45-90 CSF-A m) were drilled to recover a long sedimentary sequence, with Hole E designed to targeted gaps in recovery in Holes A and B. This research focuses on the upper 90 m of sediment, which is divided into two lithostratigraphic units: Unit I

(0-35 m; CSF-A;) is Pleistocene to Holocene age (~2.1 Ma-~5 ka) and consists of diatom-bearing/-rich mud interbedded with foraminifer-bearing sands and diamicts (McKay et al., 2019). Unit II (35-95 m CSF-A) spans the late Pliocene to early Pleistocene (~2.2-3.2 Ma) and consists of diatom-bearing/-rich mud to muddy diatom ooze interbedded with diamict (McKay et al., 2019).

Sediments recovered from Site U1523 were likely deposited by hemipelagic sedimentation, ice rafting, and downslope transport (McKay et al., 2019). Bottom currents may have influenced sediments by winnowing fines, resulting in concentrations of foraminifers in sand and diamict beds (McKay et al., 2019). This interpretation is further supported by the presence of glauconite in the sands and diamicts between 10 and 20 and from 80 to 90 m CSF-A, indicating slow sedimentation rates (Odin, 1988; López-Quirós et al., 2019). Large clasts may reflect ice rafting from icebergs entrained in the polar easterlies, downslope transport, and/or winnowing (McKay et al., 2019).

3 Materials and methods

3.1 Foraminifer sampling and preparation for geochemical analyses: Between 0 and 20 m CSF-A we sampled 20 ccs (2 cm) every ~5 cm. Between 20 and 90 m CCSF, we sampled 20 ccs (2 cm) every ~20 cm. The 20 cc samples were washed over a 65 µm sieve and the >63 um fraction was oven dried overnight at 50°C. We picked *Trifarina* sp. and *N. pachyderma* from the 125-250 and 250-355 µm size fractions. If foraminifers were present in both size fractions, we preferentially picked the larger size fraction. We picked whole tests and, whenever possible, we selected translucent glassy *Trifarina* sp. and non-encrusted *N. pachyderma (s).* We picked between 1-111 (average 17) *Trifaria* sp. and 2-195 *N. pachyderma* (average 50) tests per sample and gently crushed tests between glass slides to ensure that all chambers were opened. Samples were then homogenized with a brush and split into two aliquots for stable isotope and trace element analyses.

3.2 Foraminifer stable isotope analyses: Foraminifer tests were prepared for oxygen ($\delta^{18}O$) and carbon ($\delta^{13}C$) stable isotope analyses using standard techniques. Foraminifer fragments were rinsed with methanol, decanted, and oven dried at 50°C. Between 30 and 85 µg of foraminifer $CaCO_3$ was treated with 50°C orthophosphoric acid and generated CO_2 was analyzed at the University of South Florida College of Marine Science (USF-CMS) using a Thermo Scientific MAT 253 light stable isotope ratio mass spectrometer equipped with a Gas Bench II preparatory device. Stable isotope data were generated in random stratigraphic order. Secondary reference materials Borba, TSF-1, and LECO-$CaCO_3$ were used to correct for drift and amplitude, and normalize measurements to the Pee Dee Belemnite (PDB) scale. Reference material Atlantis-3

was used for quality control/assurance. $\delta^{18}O$ and $\delta^{13}C$ are expressed using standard delta (δ) notation in per mil (‰). Measurement uncertainty, expressed as ±1 standard deviation of n=207 measurements of the TSF-1 laboratory reference material was 0.03‰ and 0.02‰ for $\delta^{18}O$ and $\delta^{13}C$, respectively. Long-term analytical precision over the course of the study for the USF-CMS MAT 253 is 0.01‰ for $\delta^{18}O$ and 0.08‰ for $\delta^{13}C$.

3.3 Trace element/Calcium preparation and analyses

3.3.1 Foraminifer cleaning: Foraminifer $CaCO_3$ from the second sample aliquot of each sample was weighed and loaded into microcentrifuge tubes in a plexiglass cleaning rack. Initial sample weights ranged between 300 and 400 µm of $CaCO_3$. Samples were cleaned using the full oxidative and reductive cleaning protocol of Martin and Lea (2002), which is modified from Boyle and Keigwin, (1985/86), and eliminates the corrosive chelating agent DTPA to avoid Ba removal. Contamination from adherent clays was removed via rinses and ultrasonifications with deionized n-pure water (x3) and methanol (x2). Samples then underwent a reductive process to remove metal oxides (Mn- and Fe-oxides). In this step, 100 µl of a solution of hydrous (1%) hydrazine, ammonium hydroxide, and ammonium citrate was added to each vial, and caps were sealed, and the rack lid was screwed on. Racks were placed into sub-boiling hot water baths for 30 minutes; every 2 minutes, the racks were removed, flipped, ultrasonicated for 2 seconds, and returned to the water baths. This process is designed to agitate the sample, make sure the reagent gets into all parts of the sample, and discourage dissolved oxides from reprecipitating. After 30 minutes, we removed the rack lids, opened the vials, rinsed the vials and lids with n-pure water and siphoned (3x). Samples then underwent an oxidative step, using a solution of hydrogen peroxide and sodium hydroxide. We added 250 µl of the oxidative solution to each sample, capped the samples, and screwed the rack lid on. We placed the racks in the sub-boiling hot

water baths for 10 minutes; during the 10 minutes, we removed the racks at 3 and 6 minutes, flipped, and sonicated them for two seconds. After 10 minutes, we removed the rack lids, opened the vials, rinsed the vials and lids with n-pure water and siphoned (3x). Following the oxidative step, samples were transferred to acid-leached microcentrifuge tubes (submerged in warm 2N HCl for 24 hours) and treated with a weak acid leach in 0.01 M distilled HNO_3 (100 µl); vials were filled with n-pure, agitated, and siphoned (2x). Immediately prior to analysis, samples were dissolved in a standard containing all elements of interest (Sample Matrix Standard; SMS). Samples were then ultrasonicated for 10 minutes, centrifuged for 5 minutes, and loaded for analysis in random stratigraphic order.

***3.3.2 Blank and standard preparation*:** All standards were made in an Airclean 5000 Clean Bench with high-purity Spex Certiprep single element standard solutions gravimetrically combined in triple distilled 2% HNO_3. We used single element standards with concentrations of 1000 µg/mL for all elements, with the exception of Ca (10,000 µg/mL) and U (1 µg/mL), to match expected concentrations in foraminifers. All blanks and standards were stored in HDPE bottles heated in 8 M HNO_3 for ~1 hour, soaked overnight in 2 M HCl, and rinsed five times with n-pure H_2O after each cleaning step. We pipetted single element standard solutions into acid-cleaned bottles with acid-cleaned tips (flushed 3 times with distilled 2% HNO_3) and recorded the mass. To calculate concentrations, we converted mass (g) to volume (mL) using the density of each standard reported in Certificates of Analysis. All standards were made in a 2% HNO_3 blank. Trace metal grade Fisher HNO_3 was distilled for 10 hours (50 mL distilled per hour) and diluted with n-pure water. To accurately dilute to 2%, we converted weight (g) to volume (mL) using 1.51 g/cm^3 as the density of concentrated HNO_3 at room temperature (Lide, 2007).

Elemental ratios in samples were determined using a suite of standards with varying concentrations of Ca, Mg, Sr, Li, Na, Ba, U, Al, Mn, and Fe, prepared to achieve a range of elemental ratios similar to those of foraminifers (Extended data table 1A). We made four multi-element calibration standards with ~100 µg/mL Ca and increasing concentrations of all elements of interest. We designed the multi-element standards to mimic typical trace element/Ca values in foraminifers (Lea, 1999) with a focus on ratios in high-latitude foraminifers (Lear et al., 2002; Shevenell et al., 2008; Hendry et al., 2009). We performed three serial dilutions of two of the multi-element standards to monitor matrix-related effects (see section 3.4.5), and included these dilutions in calibrations lines. To ensure accurate Mg/Ca analysis, we made an additional four standards containing only Ca (~100 µg/mL) and increasing concentrations of Mg. Calibration lines for Mg and Ca thus include a total of fourteen standards ranging in concentration from 0.01-0.7 µg/mL Mg and 30-200 µg/mL Ca. To monitor accuracy, we also measured the solid carbonate reference materials ECRM 752-1 (Bureau of Analyzed Samples Ltd, UK), BAM RS3 (Bundesanstalt fur Materialforschung und -prufung, Germany), and CM 1767 (China Metallurgical Standardization Research Institute, Beijing) at a Ca concentration of ~100 µg/mL. Finally, we added Yttrium (Y) to all standards to match the Y concentration in the SMS (~20 ng/mL). In hindsight, we recognize that a more efficient method would include spiking the blank with Y and using the Y-spiked blank to make all standards and dissolve samples.

3.3.3 Instrumentation: Minor and trace elements were measured between March and June, 2020 (23 runs) on the USF-CMS Thermo Element Extended Range Inductively Coupled Plasma Mass Spectrometer (XR ICP-MS) fitted with Thermo Scientific nickel sample and skimmer cones. The XR ICP-MS is equipped with an ESI SC-4 DX autosampler, and we used a concentric PFA-ST microflow nebulizer and a quartz cyclonic spray chamber for sample introduction. We calculated

flow rate after tuning and prior to the start of each run, and found an average of ~120 μL min^{-1} (n=23) over the four-month analysis interval. Prior to each run, we cleaned cone orifices with a soft brush to remove metal deposits that could block ion transmission. All isotopes were measured in low resolution (R=300), with the exception of ^{45}Sc, ^{55}Mn, and ^{56}Fe, which were measured in medium resolution (R=4000) to avoid spectral interferences. We measured all isotopes in analog mode to avoid errors associated with cross-calibration (Rosenthal et al., 1999). We report Mg/Ca from ^{24}Mg due to its high natural abundance and ratio all minor and trace elements to ^{43}Ca. Mg/Ca is on average ~1% greater when calculated from ^{24}Mg compared to ^{25}Mg, which may relate to potential interference on ^{24}Mg from ^{48++}Ca. A typical run sequence consisted of 30 unknowns and standard blocks run at the beginning, middle, and end (Extended data figure 1A).

3.3.4 Data processing: We observed progressively lower signals (counts per second; cps) in standards throughout each run, likely due to changes in instrument performance and/or metal deposition on cones. To correct for drift, we applied an internal standard factor on samples and standards cps, defined as the ratio between the ^{88}Y in the first sequence line to the ^{88}Y in each subsequent sequence line. We divided each isotope measurement by the sequence line-specific internal standard factor. This correction is predicated on the assumption that isotopes of interest (^{43}Ca, ^{24}Mg, etc.) react to changing instrument conditions in the same manner as ^{88}Y. We observed slightly different drift patterns in standards and samples, because we individually spiked standards with Y, and dissolved samples with the same solution of the Sample Matrix Standard (SMS). To correct for different drift patterns, we treated standards with an internal standard factor based on the first sequence line of the run, and samples with a factor based on the first SMS measurement.

We ran the SMS after every third sample, and removed the influence of SMS on samples by subtracting the average isotope signal in bracketed SMS from sample isotopes in cps. We then converted raw counts to concentrations using linear calibration lines. To remove the influence of the blank on standards and samples, we included blank measurements in calibration lines. We used isotopic concentrations in calibration lines and subsequently converted isotopic to elemental concentrations using natural isotope abundances. Across all runs, coefficients of determination (R^2) for Mg and Ca calibration lines are >0.99, and between 0.95-0.99 for other elements of interest, with the exception of Al. We observed noise in Al calibration lines when testing the multi-element ratio standards, and thus prepared three additional single element Al standards for calibrations. Coefficients of determinations for single element Al standards were initially good (0.94), but degraded over the course of the study interval (average 0.82).

The relative standard deviation (RSD) for Mg/Ca in SMS across all runs, an indicator of long-term precision, is 5.7% (n=188). To improve precision, we applied a noise correction factor to sample trace element (TE) ratios using the ratio between known and measured concentrations in the SMS bracketing samples (Schrag, 1999; Rosenthal et al., 1999):

$$(TE/Ca)_{corrected\ sample} = (TE/Ca)_{uncorrected\ sample} * (Actual\ TE/Ca)_{SMS} / (Average\ measured\ TE/Ca)_{SMS}$$

This correction lowers the RSD of all SMS Mg/Ca measurements to 1.1%, which is comparable to standard solution Mg/Ca RSDs of Yu et al. (2005) and Lear et al. (2010) (~1%), but greater than those calculated by de Villiers et al. (2002) (<0.3%), Rosenthal et al. (2004) (0.3-0.5%), and Marchitto (2006) (0.55%).

We monitored Mg/Ca accuracy and precision with the community reference materials ECRM 752-1, BAM RS3, and CM 1767 (Table 1; Greaves et al., 2008). Measured Mg/Ca of

calibrated and noise corrected reference materials are ~2-4% higher in this study than the interlaboratory mean in Greaves et al. (2008) (Table 1).

Table 1: Measures of accuracy and precision in Mg/Ca reference materials. Mean Mg/Ca are based on measurements across the four-month analysis period (n=67 per standard).

Reference material	Mean Mg/Ca (mmol/mol) This study	Mean Mg/Ca (mmol/mol) Greaves et al. (2008)	RSD (%)
ECRM 752-1	3.91	3.75	2.9
BAM RS3	0.80	0.78	2.6
CMSI 1767	5.69	5.59	3.0

3.3.5 Matrix effects: Changes in the composition (matrix) of samples can cause deviations between measured and actual Mg/Ca in mass spectrometry (Rosenthal et al., 1999; Lear et al., 2002; de Villiers et al., 2002). To monitor matrix-related mass discrimination, we measured four serial dilutions of two multi-element standards with Mg/Ca values similar to those predicted for Antarctic foraminifers (Figure 4). In the absence of matrix effects, standard dilutions should have the same Mg/Ca values despite varying Mg and Ca concentrations. Instead, there is a significant matrix effect on Mg/Ca (R^2= 0.6-0.7) in standards with higher Mg/Ca values, which reflect higher Ca concentrations. This relationship is the opposite of the negative relationships between Mg/Ca and Ca concentration found by Rosenthal et al. (1999), Lear et al. (2002), de Villiers et al. (2002), and Marchitto (2006). We removed matrix effects on sample Mg/Ca via corrections based on the ratio of known Mg/Ca to measured Mg/Ca in the Sample Matrix Standard (Rosenthal et al., 1999; Schrag, 1999) and in community standards (Greaves et al., 2008).

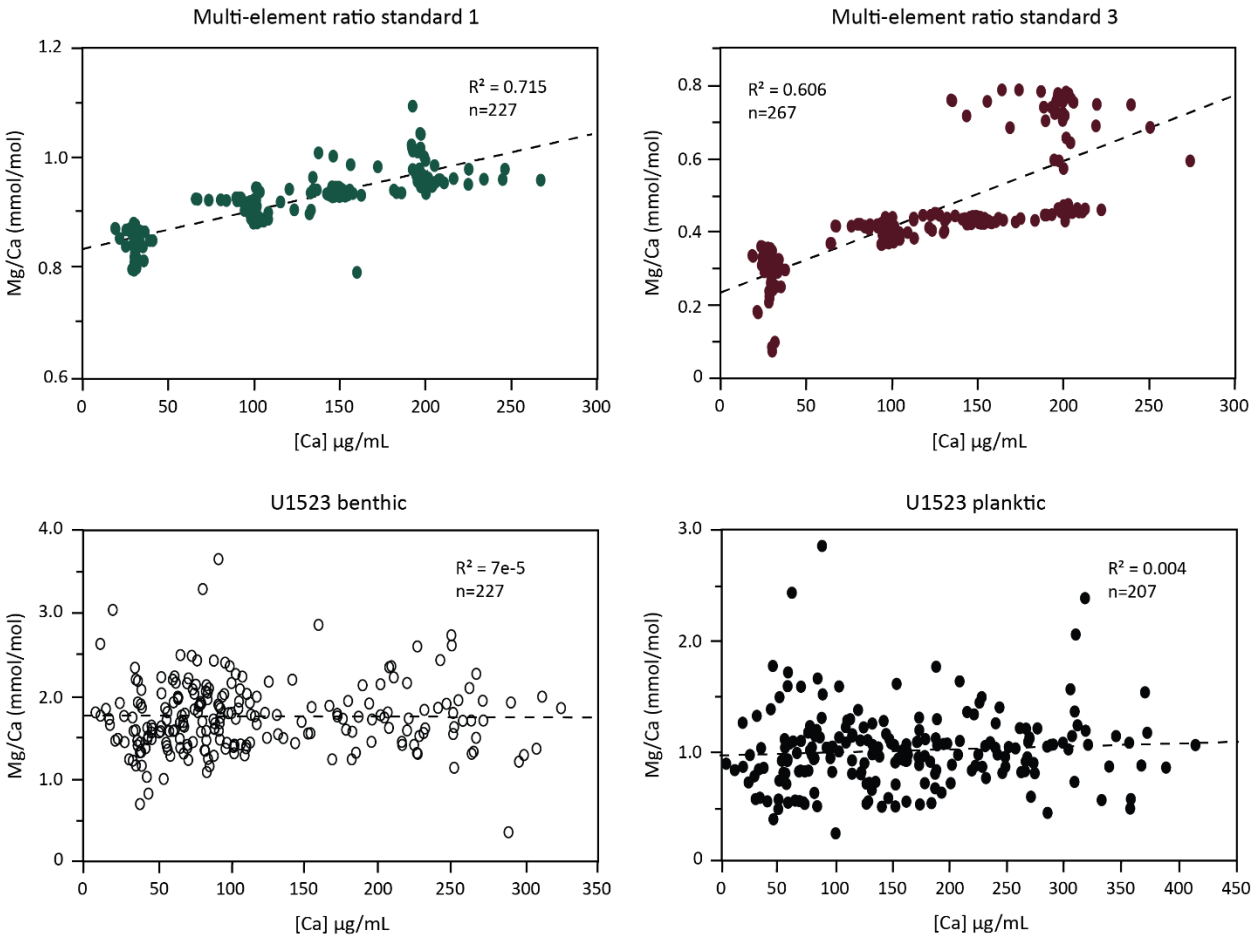

Figure 4: Calcium matrix effects on Mg/Ca in standards and samples. Measured Mg/Ca (mmol/mol) is shown as a function of measured Ca concentration (µg/mL) in two multi-element ratio standards (top) and all U1523 benthic and planktic samples (bottom). Multi-element ratio standards were diluted to expected Ca concentrations of ~200, 100, 150, and 30 µg/mL. In the bottom panel, sample Mg/Ca have undergone corrections that account for matrix-effects. Standards and samples were run over a four-month period (March-June 2020).

4 Composite depth scale

We correlated Holes U1523A, B, and E to construct a composite depth scale in the top 90 m of Site U1523, which maximizes coverage by accounting for gaps in core recovery, coring offsets, and disturbance. We correlated cores with X-ray fluorescence (XRF) Rb/Sr, Ca/Ti, Br/Ti, and Zr/Rb counts across holes in Igor Pro software (Wavemetrics, Inc.) with Code for Ocean Drilling Data (Wilkens et al., 2017). XRF counts were measured on the Avaatech XRF Core Scanner at the IODP Gulf Coast Repository (Texas, USA), at 10, 30, and 50 kV, with measurements taken every 1-2 cm. After correlating cores with XRF data, we used Zr/Rb and MS to identify the least disturbed portion of overlapping cores to develop the composite section (Extended data figures 2A and 3A). The splice alternates between Holes A and E in the top 40 m and between Holes E and B from 40-90 m CSF-A (Extended data table 2A). We added offsets to the original CSF-A core depths to create the core composite below sea floor (CCSF; IODP-MI, 2011) depth scale.

5 Chronology

5.1 Shipboard chronology: The IODP Expedition 374 Shipboard Scientific Party developed a preliminary chronology for Site U1523 based on biostratigraphic and paleomagnetic datums (McKay et al., 2019) (Figure 5). In the top 25 m of Site U1523, biostratigraphic control is poor due to reworked microfossils. A single radiolarian Last Appearance Datum (LAD; *Antarctissa cylindrica*) exists within the upper 10 m of Hole U1523E, and is assigned an age of <0.65 Ma (McKay et al., 2019). A possible unconformity was identified in the same hole at ~20 m CSF-A (McKay et al., 2019). A magnetic reversal at ~19 m CSF-A may represent either the base of the Brunhes Chron (0.78 Ma) or the Jaramillo Subchron (1.07 Ma); the reversal was not included in the shipboard age model due to insufficient biostratigraphic support (McKay et al., 2019). Two magnetic reversals with good biostratigraphic age control constrain the top of the Olduvai Chron (1.8 Ma) and Subchron C2r.2r (2.6 Ma) (Table 2). An unconformity at ~95 m CSF-A is estimated to be between ~8.5-3.2 Ma and interpreted as Ross Sea Unconformity 3 (RSU3; McKay et al., 2019; Conte et al., submitted).

5.2 Shorebased chronology: To improve the chronology in the top 16 m CCSF of Site U1523, we tied Site U1523 MS and Natural Gamma Radiation (NGR) records to the MS record of a nearby sediment core (RS15-GC41; Kim et al., 2020) (Figure 6) (Table 2). Kim et al. (2020) established the chronology for RS15-GC41 with foraminifer radiocarbon (^{14}C) dates and δ^{18}O, and by tying low MS values to interglacial Marine Isotope Stages (MIS) of the global benthic LR04 δ^{18}O stack (Lisiecki and Raymo, 2005). High MS during glacial periods is corroborated by two ^{14}C dates from Site U1523 at 0.47 m CCSF (21 Kyr) and 0.72 m CCSF (32 Kyr), which

places the Last Glacial Maximum in an interval of high MS and NGR. The temperate planktic foraminifer species *Globigerina bulloides* is present in U1523 during some low MS intervals (Seidenstein, 2020) (Figure 6). Because *G. bulloides* occupies a range north of U1523 in warmer subpolar waters (Bé and Tolderlund, 1971; Fillon, 1974), its presence supports the interpretation that low MS reflects interglacials conditions.

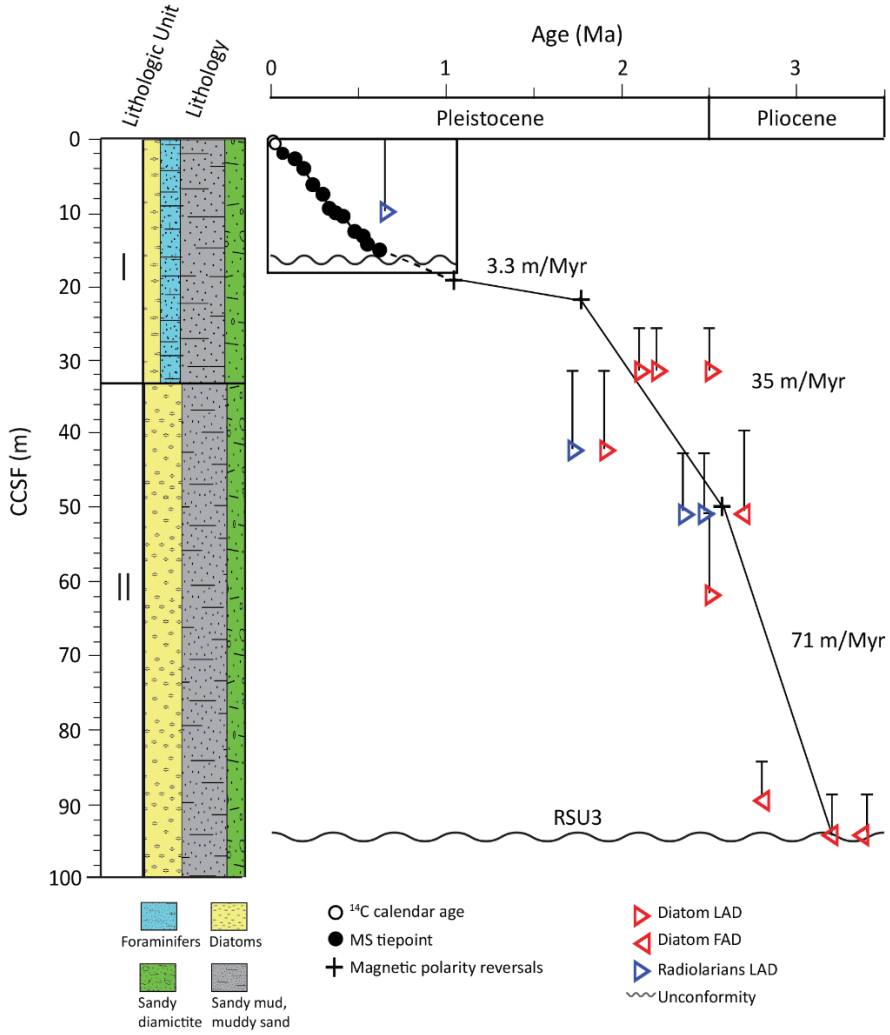

Figure 5: Lithology and chronology in the U1523 Plio-Pleistocene sequence. The U1523 Plio-Pleistocene sequence is divided into two lithostratigraphic Units, differentiated by the prevalence of foraminifer-bearing muddy sand and diamict in Unit I, and diatom-bearing muds and oozes in Unit II (McKay et al., 2019). Linear age models were developed based on foraminifer ^{14}C dates, Magnetic Susceptibility (MS) correlations, and paleomagnetic reversals from U1523E 3F-2 (C1r.1n; 19 m CCSF) U1523E 4F-1 (C1r.3r/C2n; 22 m CCSF) and U1523B 3F-2

(C2r/C2An; 50 m CCSF) (Table 2). Diatom first (FAD) and last appearance datums (LAD) were used to constrain the ages of paleomagnetic reversals. Unconformities exist at ~16 m and 95 m CCSF, the latter interpreted as Ross Sea Unconformity 3 (RSU3). Sedimentation rates are listed as meters per million year (m/Myr). The box in Unit I highlights the interval in Figure 6.

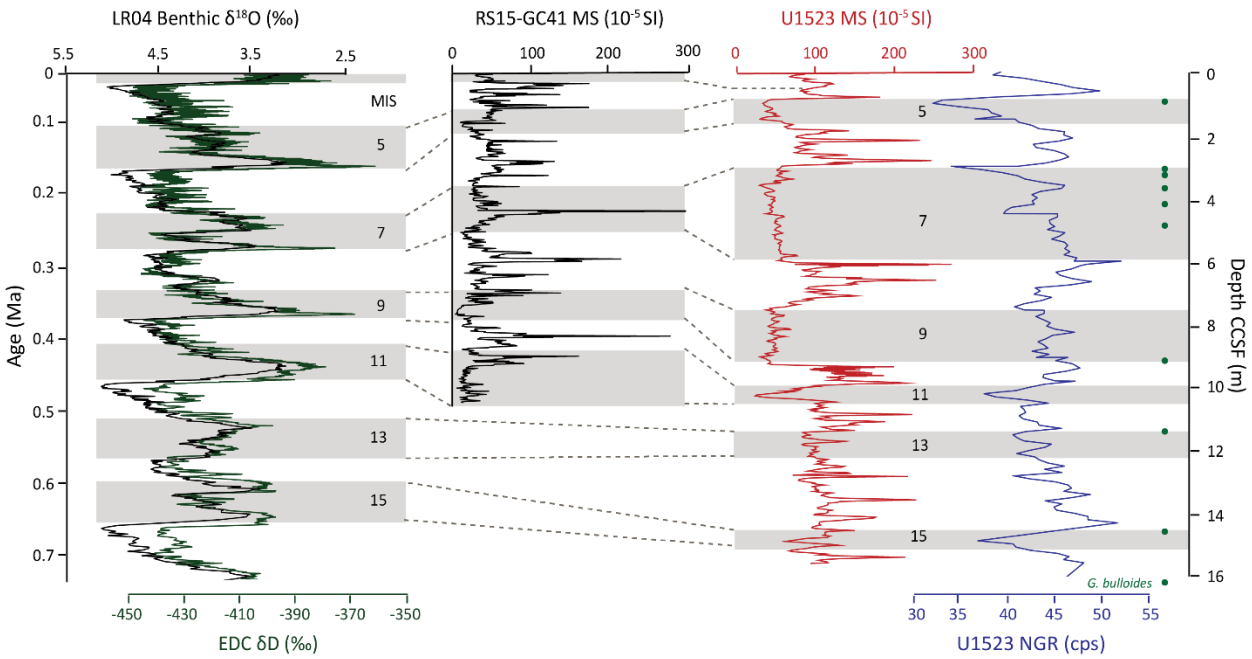

Figure 6: Revised mid-late Pleistocene chronology in the top 16 m CCSF. To improve age control in the top 16 m CCSF we tie MS in U1523 to RS15-GC41, a sediment core from the Iselin Bank tied to the global benthic $\delta^{18}O$ stack (LR04) (Figure 3; Kim et al., 2020; Lisecki and Raymo, 2005). Also shown is the EPICA Dome C (EDC) ice core deuterium (δD) record (Jouzel et al., 2007), U1523 Natural Gamma Radiation (NGR) cps, and U1523 sample depths containing the temperature planktic foraminifer species *Globigerina bulloides*. Interglacial Marine Isotope Stages (MIS) are highlighted.

We determined depths for warm Marine Isotope Stages 5 through 11 by correlating low MS and NGR in U1523 to low MS in RS15-GC41 (Figure 6). We tied the tops and bottoms of low MS intervals to the beginning and end of interglacials according to the LR04 chronology (Lisiecki and Raymo, 2005) (Figure 6). Extended intervals of high and low MS are easily assigned to glacial and interglacial stages in the top 10 m of U1523. MIS 7 is a particularly

prolonged and warm interglacial, based on a 3 m sequence of mud and silts containing *G. bulloides* in five samples (Figure 6). We assign MIS 11 to a condensed interval of low MS and NGR. From 16-10.5 m CCSF, discrete fluctuations in relatively high MS obscures cycles, and NGR progressively decreases upsection from ~14 to 10.5 m CCSF (U1523A 4H-2H), suggesting an extended glacial to interglacial transition. We assign MIS 13 and 15 to intervals within this sequence with low MS, high $CaCO_3$, and *G. bulloides* tests. We assign the magnetic reversal downcore (~19 m CCSF) to the Matuyama/Jaramillo reversal (1.07 Ma). Depths are converted to age using linear interpolations between age control points (Figure 5).

Table 2. U1523 age control points. We performed linear interpolations between age control points to assign depths to ages. MS= magnetic susceptibility.

Depth CCSF (m)	Age (Ma)	Chronology data type
0.5	0.021	^{14}C in foraminifers
0.7	0.032	^{14}C in foraminifers
0.9	0.072	MS tie
1.8	0.13	MS tie
3.0	0.19	MS tie
5.9	0.24	MS tie
7.5	0.31	MS tie
9.3	0.34	MS tie
10.1	0.39	MS tie
10.4	0.42	MS tie
11.3	0.48	MS tie
12.4	0.53	MS tie
14.8	0.57	MS tie
15.5	0.62	MS tie
19.3	1.1	Magnetic chron C1r.1n
21.7	1.8	Magnetic chron C1r.3r/C2n
49.7	2.6	Magnetic chron C2r/C2An
93.9	3.2	First appearance of *Thalassiosira vulnifica*

6 Results

6.1 Foraminifer stable isotopes: We present stable oxygen ($\delta^{18}O$) and carbon ($\delta^{13}C$) isotopes in *Trifarina* (n=215) and *N. pachyderma* (n=275) from the top 90 m CCSF of Site U1523 (Figure 7). Isotope resolution is best in the top 25 m CCSF due to high sediment recovery and $CaCO_3$ content. From 0 to 25 m CCSF, benthic foraminifer stable isotope resolution is ~1 sample/10 cm (9 Kyr) and from 25 to 90 m CCSF, isotope resolution is ~1 sample/30 cm (25 Kyr). We removed two planktic samples from isotope datasets due to clearly outlying $\delta^{18}O$ measured on few foraminifers. We replicated measurements on 20% of samples and show average values in all figures.

6.1.1 Oxygen Isotopes ($\delta^{18}O$): *Trifarina* and *N. pachyderma* $\delta^{18}O$ increases by 1.3‰ and 1.4‰ upsection through the 90 m sequence, which is consistent with deep-sea benthic foraminifer $\delta^{18}O$ evidence of a ~1.5-1.7‰ increase across the last 3 Ma (Lear et al., 2000; Billups and Schrag, 2002; Lisiecki and Raymo, 2005). This U1523 foraminifer $\delta^{18}O$ increase is slightly lower than in deep-sea records due to the influence of low $\delta^{18}O$ meteoric waters from the nearby Ross Ice Shelf. *Trifarina* $\delta^{18}O$ is, on average, more positive than *N. pachyderma* (4.9 ± 0.1‰) and ranges from 3.4‰ (87 m CCSF; 3.1 Ma) to 5.7‰ (7 m CCSF; 0.28 Ma). Average *N. pachyderma* $\delta^{18}O$ is 4.6 ± 0.1‰ and varies between 2.8‰ (87 m CCSF; 3.1 Ma) to 5.2‰ (8 m CCSF; 0.31 Ma). Researchers have found an offset between predicted and measured $\delta^{18}O$ in *N. pachyderma* of ~1.0‰ (Kohfield et al., 1996; Bauch et al., 1997; Volkmann and Mensch, 2001; Smith et al., 2005; Nyland et al., 2006). However, these vital effect estimates are all derived from North Atlantic and Arctic Ocean *N. pachyderma,* and ignore influences on stable isotope incorporation

specific to Antarctic shelves. We therefore do not apply a pre-existing vital effect correction to Ross Sea *N. pachyderma* stable isotope records.

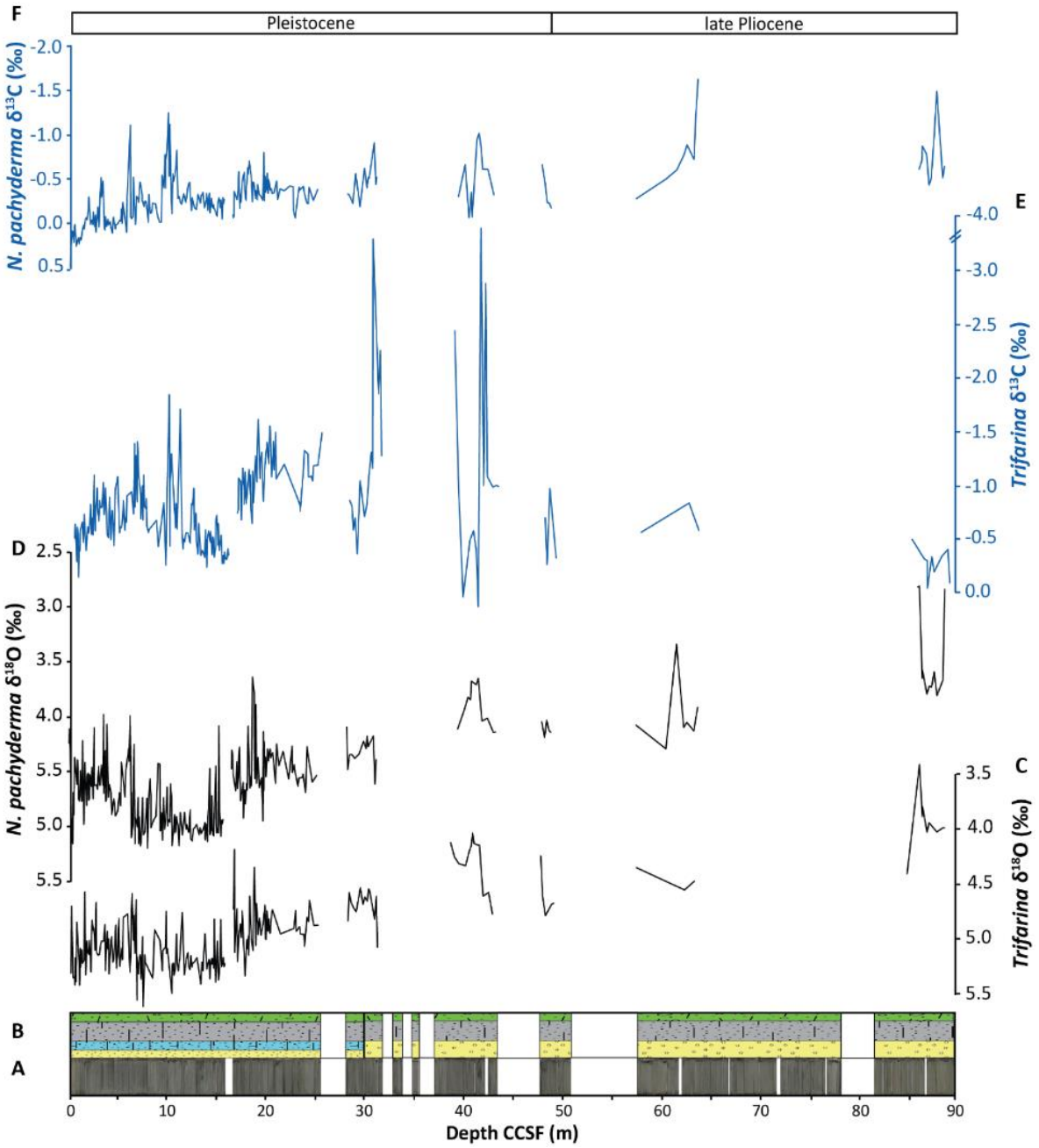

Figure 7: Foraminifer δ^{18}O and δ^{13}C from U1523 spanning the Plio-Pleistocene. (A) core photos and (B) lithologic graphic, which reflects the predominance of foraminifers in muddy sands and diamict in Unit I (~33-0 m CCSF), and diatom-bearing muds and oozes in Unit II (McKay et al., 2019). Lithology legend is in Figure 5. White spaces represent gaps in sediment recovery, and are inferred to reflect unconsolidated sands and gravels. (C) benthic

Trifarina sp. and (D) planktic *Neogloboquadrina pachyderma* (sinistral) $\delta^{18}O$, and (E) benthic and planktic (F) $\delta^{13}C$. Isotope resolution is best in the top 25 m CCSF (1.9-0 Ma) (see Figure 8 for high resolution isotopes from 25-0 m).

Fluctuations are superimposed on the long-term ice growth and cooling trend. If these spikes are not a relic of sample aliasing, they may reflect local variations in Ross Sea temperature and ice volume. The upsection $\delta^{18}O$ increase is interrupted by low *Trifarina* and *N. pachyderma* $\delta^{18}O$ from 43-41 m CCSF (2.4-2.3 Ma) and 19-17 m CCSF (1.1-0.9 Ma) (Figure 7). At these depths $\delta^{18}O$ values are similar to those at the base of the sequence, suggesting a return to climate and oceanographic conditions similar to the warm Pliocene during the early and mid-Pleistocene. In the former interval at ~41 m CCSF, decreasing $\delta^{18}O$ occurs in samples containing *G. bulloides*, indicating relatively warm waters at Site U1523 (Seidenstein, 2020). The latter interval (19-17 m CCSF) is characterized by large *Trifarina* and *N. pachyderma* $\delta^{18}O$ fluctuations of up to 1.0‰ and 1.5‰. *Trifarina* and *N. pachyderma* $\delta^{18}O$ increases abruptly by 0.5‰ and 0.8‰ from 17 to 16 m CCSF. This rapid shift in $\delta^{18}O$ is mirrored in $\delta^{13}C$ records (Figure 7). A final trend toward lower $\delta^{18}O$ occurs at 4.9 m CCSF (0.21 Ma) where $\delta^{18}O$ in both species decreases by ~0.7‰.

6.1.2 Carbon isotopes ($\delta^{13}C$): Large fluctuations in *Trifarina* $\delta^{13}C$, ranging from -3.7‰ (41.5 m CCSF) to 0.16‰ (41.1 m CCSF), occur between 42 and 30 m CCSF (2.0-2.4 Ma) (Figure 7). *Trifarina* $\delta^{13}C$ values are <-1.5‰ in seven samples within this interval; more negative *N. pachyderma* $\delta^{13}C$ values (<-1.0‰) also occur at 41.9, 41.5, and 35.3 m CCSF. In the high-resolution foraminifer record in the top 25 m, *Trifarina* $\delta^{13}C$ fluctuations are much more subtle, ranging from -1.8‰ (9.7 m CCSF) to -0.12‰ (0.45 m CCSF).

The average $\delta^{13}C$ in *N. pachyderma* (-0.48‰) is more positive than in *Trifarina* (-0.79‰), and *N. pachyderma* exhibits more muted negative $\delta^{13}C$ excursions, ranging from -2.0‰ (64 m CCSF; 2.8 Ma) to 0.48‰ (0.1 m CCSF; 30 Kyr) across the 90 m sequence. Pliocene $\delta^{13}C$

values are generally more negative in *N. pachyderma* and positive in *Trifarina* compared to the Pleistocene. *N. pachyderma* $\delta^{13}C$ exhibit an overall upsection increase of ~1.3‰. Low *N. pachyderma* $\delta^{13}C$ from 89-87 m CCSF occurs in small (250-125 µm) individuals, and may reflect the positive relationship between test size and $\delta^{13}C$ in planktic foraminifers (Elderfield et al., 2002). The $\delta^{13}C$ in both species steadily increases prior to the mid-Pleistocene unconformity from 21-17 m CCSF (1.6-0.8 Ma). *Trifarina* $\delta^{13}C$ exhibits a distinct increase by ~0.5‰ above the mid-Pleistocene unconformity at 16 m CCSF. Two more intervals of particularly negative $\delta^{13}C$ occurs in benthics and planktics from 11-10 m CCSF (0.44-0.35 Kyr) and at ~6 m CCSF (0.24 Ma), below which is an upsection $\delta^{13}C$ increase toward the Site U1523 coretop beginning at ~3 m CCSF (0.15 Ma) in *Trifarina* and 2 m CCSF (60 Kyr) in *N. pachyderma*.

We interpret the abrupt shift in isotope records at 16 m CCSF to be the depth of the unconformity assigned to 20 m CSF-A in the shipboard age model. Based on overlying MS tiepoints, we estimate ~1 Ma missing in unconformity across MIS 16 (0.75-0.65 Ma). This corresponds to the estimated age of RSU1 (0.65 Ma) in DSDP Leg 28 Sites 270, 272, and 273 (Hayes and Frakes, 1975; Savage and Ciesielski, 1983). In the AND-1B site drilled north of U1523, an unconformity at ~0.78 Ma, together with a major shift in sedimentary facies, is associated with more persistent ice shelves during late Pleistocene interglacials (McKay et al., 2012b). MIS 16 is thus tentatively assigned to the unconformity at 16 m CCSF, because MIS 16 marks the end of the MPT in deep-sea $\delta^{18}O$ records (Mudelsee and Schulz, 1997).

6.2 $\delta^{18}O$, $\delta^{13}C$, and MS records from 0-25 m CCSF: MS is a reliable recorder of grain size in U1523, and thus can be used to infer changes in bottom current strength. In the top 25 m of U1523, high MS intervals are characterized by foraminifer-bearing/rich sand and diamict facies deposited under high velocity currents, whereas low MS reflects diatom-bearing/rich muds

deposited via hemipelagic sedimentation under slow currents. Samples from low MS intervals contain few foraminifers, which are concentrated in the smaller size fraction (250-125 μm). Foraminifers predominance in coarse grained sediment may be due to winnowing by strong bottom currents, nutrient delivery via mCDW (Osterman and Kellogg, 1979), and/or enhanced $CaCO_3$ preservation due to fast-moving currents removing detrital material that would otherwise undergo respiration and contribute to corrosivity (Kennett, 1968; Prothro et al., 2018).

High-resolution isotope records in the upper 25 m of Site U1523 allows us to trace the relationship between MS, $\delta^{18}O$, and $\delta^{13}C$ (Figure 8). We broadly delineate three intervals in the top 26 m based on MS and isotope patterns. Benthic and planktic $\delta^{18}O$ is generally highest in the deepest interval (25-17 m CCSF), indicating warmer ocean temperatures and reduced ice volume relative to upsection. An extended period of low MS (~23-19 m CCSF) is bounded by coarse grained facies. Immediately above the inferred unconformity (~19-18 m CCSF) fluctuations in MS pair well with isotopes, with low $\delta^{18}O$ and $\delta^{13}C$ values occurring in high MS sediment. Below the unconformity, large negative peaks in *N. pachyderma* $\delta^{18}O$ yield to an interval of low variability in MS and $\delta^{18}O$ from ~14-11 m CCSF. Relatively uniform isotope values are disrupted by a rapid decrease in planktic and benthic $\delta^{13}C$ at 11 m CCSF and more negative planktic $\delta^{18}O$. A condensed interval of low MS at 10.3 m CCSF (MIS 11) pairs with a brief increase in $\delta^{13}C$ and *Trifarina* $\delta^{18}O$. The base of the upper highlighted interval (9.3-0 m CCSF) is marked by an abrupt return to more positive $\delta^{13}C$ values. This upper interval is characterized by extended MS sequences similar to downsection (25-16 m CCSF) and low $\delta^{18}O$ and $\delta^{13}C$ values bounding high MS intervals.

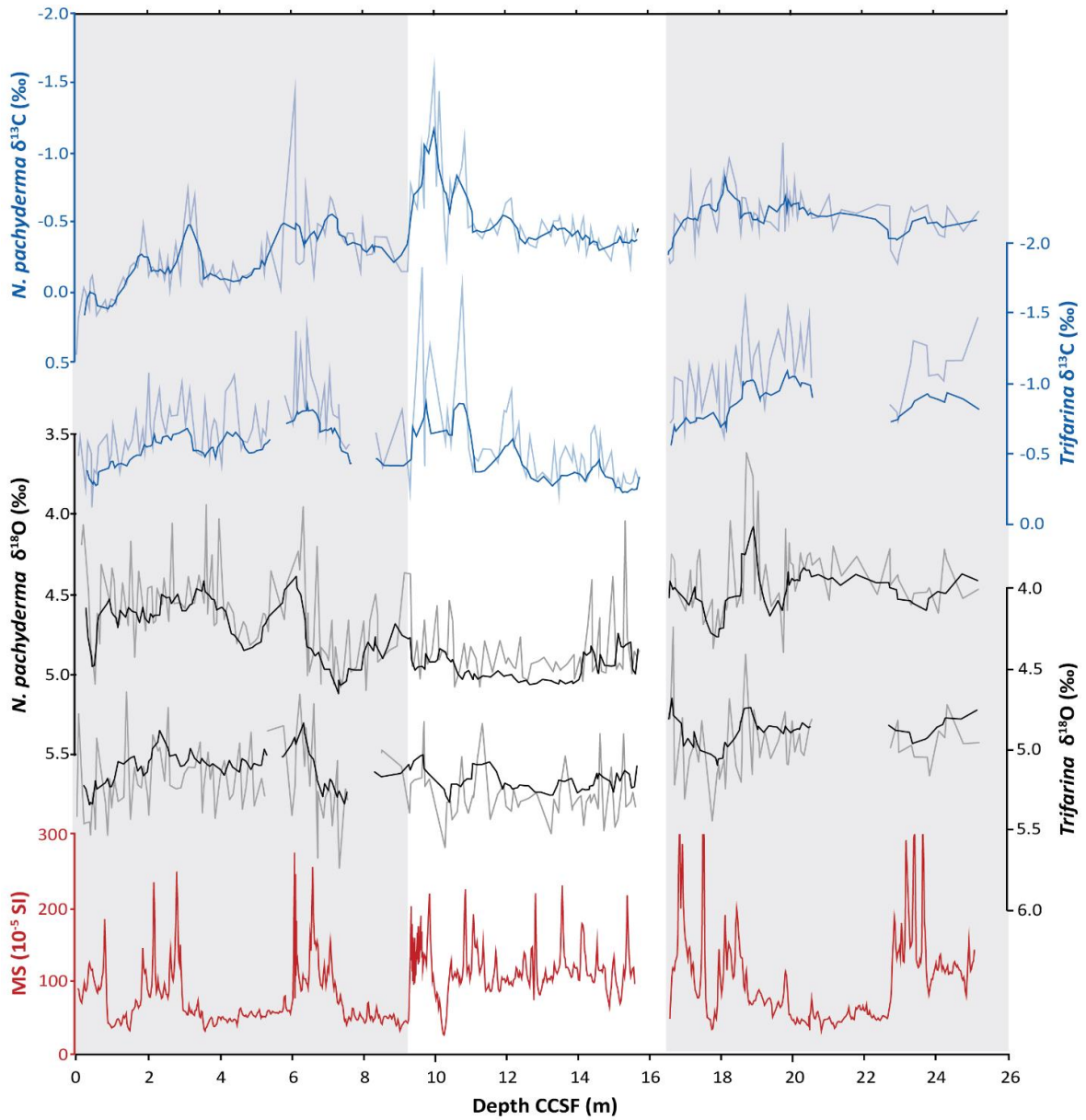

Figure 8: High-resolution MS and isotopes in the top 25 m CCSF (1.9-0 Ma) of U1523. Bold lines are 5-point moving averages. Vertical grey bars delineate broad oceanographic and climate states in the Ross Sea evident in isotope and lithographic records.

6.3 Foraminifer Mg/Ca

6.3.1 Monitoring Mg/Ca contaminants: We measured Mn, Fe, and Al to assess the post-cleaning influence of secondary mineral phases and aluminosilicates on Mg/Ca. Authigenic Mn and Fe-rich carbonate coatings in foraminifer tests are associated with high Mg concentrations

(Boyle, 1983; Martin and Lea, 2002; Pena et al., 2005), and are a major source of contamination in Mg/Ca-temperature reconstructions (Lea, 1999). U1523 interstitial water profiles document increasing Mn concentrations from 90-0 m (McKay et al., 2019), indicating Mn^{2+} release and migration through pore waters in the suboxic-anoxic transition zone (Boyle, 1983). Mn/Ca and Fe/Ca in U1523 foraminifers are higher than the >0.1 mmol/mol threshold set by Barker et al. (2005) and Lear et al. (2010) (Figure 9). *Trifarina* Mg/Ca values are not correlated with contaminant indicators, and *N. pachyderma* Mg/Ca values are weakly correlated with Mn/Ca and Fe/Ca.

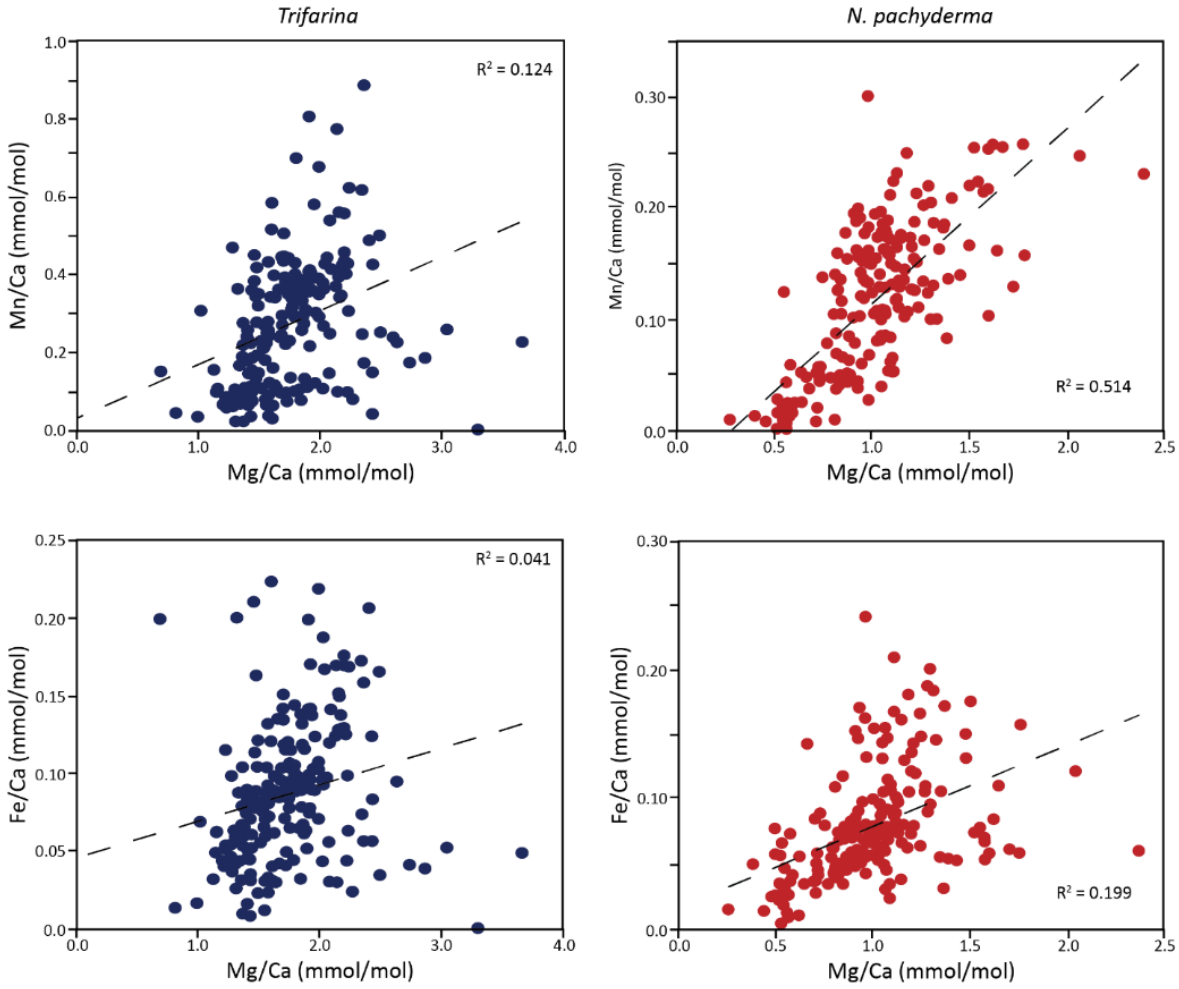

Figure 9: Linear correlations between Mg/Ca, Mn/Ca and Fe/Ca in foraminifers. Top panel shows Mn/Ca and bottom panel is Fe/Ca. Relationships in benthic *Trifarina* are shown in blue and planktic *N. pachyderma* in red.

Coefficients of determination demonstrate statistically significant relationships between Mg/Ca and contaminant indicators in *N. pachyderma*.

6.3.2 ***Mg/Ca in the top 25 m CCSF:*** We present Mg/Ca in benthic *Trifarina* (n=219) and planktic *N. pachyderma* (n=188) from the upper 25 m of U1523 (Figure 10). Mg/Ca resolution for *Trifarina* is ~1 sample/13 cm (10 Kyr), and for *N. pachyderma,* ~1 sample/14 cm (10 Kyr). We removed 20 benthic and planktic Mg/Ca data due to low sample weights, high Fe, Mn, and/or Al concentrations, and outlying Mg/Ca. Replicates were measured on 31% and 48% of benthic and planktic samples and used to calculate standard deviations. Benthic Mg/Ca is on average 1.76 ± 0.16 mmol/mol and ranges between 1.3 (17.6 m CCSF; 0.9 Ma) to 3.6 (3 m CCSF; 0.17 Ma) mmol/mol. Planktic Mg/Ca is on average 1.0 ± 0.10 mmol/mol and ranges between 0.3 (5 m CCSF; 0.21 Ma) to 2.9 mmol/mol (9.9 m CCSF; 0.36 Ma).

Benthic and planktic Mg/Ca fluctuations accompany changes in MS and $\delta^{13}C$. Benthic Mg/Ca is generally high in sands and diamicts indicated by high MS (Figure 10). Planktic Mg/Ca and $\delta^{13}C$ are well correlated (R^2=0.42) and high planktic Mg/Ca (>2 mmol/mol) occur in intervals of low $\delta^{13}C$ (<-1‰) (11 and 10 m CCSF). Mg/Ca in benthic and planktics do not consistently track $\delta^{18}O$. For example, the shift in $\delta^{18}O$ toward more positive values above the 16 m CCSF unconformity is not accompanied by lower benthic Mg/Ca. Planktic Mg/Ca does decrease above 16 m CCSF by ~0.2 mmol/mol, but planktic Mg/Ca and $\delta^{18}O$ changes do not track at 8 m CCSF, where Mg/Ca decreases by ~0.6 mmol/mol upsection, despite $\delta^{18}O$ becoming more negative.

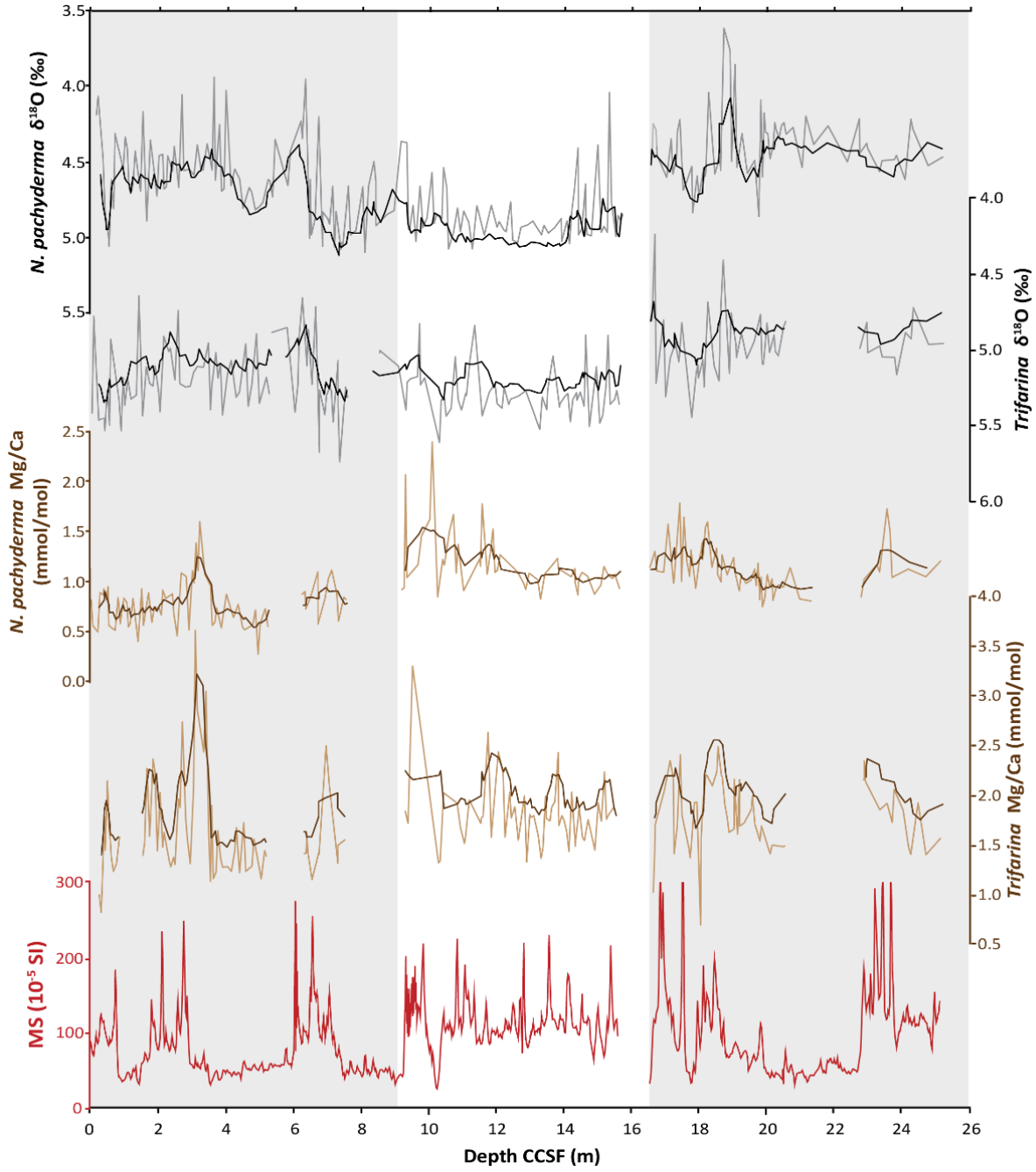

Figure 10: MS, Mg/Ca, and $\delta^{18}O$ in the top 25 m CCSF (1.9-0 Ma). Bold lines are 5-point moving averages. Vertical grey bars are identical to the those in Figure 7.

7 Discussion

7.1 Fidelity of stable isotopes and Mg/Ca measurements:

7.1.1 Mg/Ca-temperature calculations: We generate U1523 bottom and surface water temperature records with genus and species-specific Mg/Ca temperature calibrations (Figure 11). We convert Mg/Ca to temperature with the *Uvigerina* sp. calibration of Elderfield et al. (2010), which is linear because of a low temperature range in Antarctic bottom waters, and *Uvigerina's* relatively low temperature sensitivity. Nürnberg (1995) first developed a high latitude Mg/Ca-temperature calibration for planktic *N. pachyderma,* which was refined by Elderfield and Ganssen (2000). To reconstruct surface water temperatures, we used the calibration of Vázquez Riveiros et al. (2016), which incorporates data from the two aforementioned calibrations, and covers the Plio-Pleistocene sea surface temperature range reconstructed by McKay et al. (2012a). There is a weak correlation (R^2= 0.35) between Mg/Ca and temperature in *N. pachyderma* when Southern Ocean sites close to the sea ice edge are included in the Vázquez Riveiros et al. (2016) calibration. This relationship improves when sites close to Antarctica are excluded from the calibration (R^2=0.70), suggesting a poor response of Mg/Ca to temperature in ice-proximal *N. pachyderma*. We thus calculated surface water temperatures with the Vázquez Riveiros et al. (2016) calibration that excludes cores close to sea ice (Figure 11). We applied the temperature calibrations of *Trifarina* (Elderfield et al., 2010) and planktic *N. pachyderma* (Vázquez Riveiros et al., 2016) to Mg/Ca measured in the reference material BAM RS3, the community standard with Mg/Ca closest to those expected in Antarctic foraminifers, and average standard deviations

(n= 67) translate to a temperature error of ~0.35ºC, which is well within the temperature calibration errors.

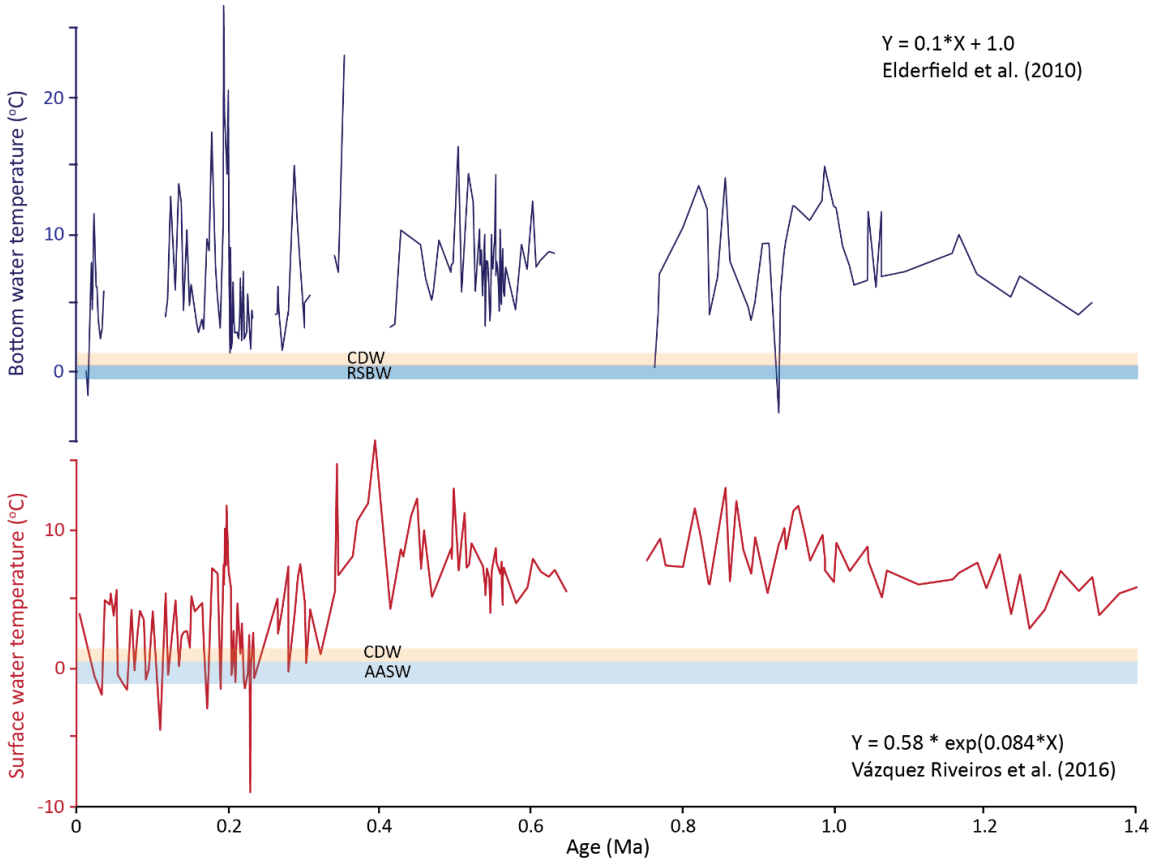

Figure 11: Mg/Ca-temperatures spanning the last 1.4 Ma. Horizontal bars highlight the present-day temperature ranges of AASW (-1.0-0.5ºC), CDW (-0.5-1.5ºC), and RSBW (-0.5-0.50ºC) at U1523 (Conte et al., submitted). Equations are the calibrations used to convert Mg/Ca to temperatures.

U1523 *Trifarina* and *N. pachyderma* Mg/Ca values are high and convert to warm temperatures that exceed 10ºC (Figure 11). Mg/Ca-bottom water temperature reconstructions are consistently higher than modern temperature estimates at U1523, and reach maxima of ~27ºC. Mg/Ca-surface water temperatures are also elevated compared to present-day estimates, but decrease to more reasonable values beginning at 0.32 Ma. U1523 Mg/Ca-surface water temperatures in older sediment (3.2-2.0) Ma are also higher (3-12ºC) than TEX_{86}-surface

temperature reconstructions from AND-1B in the Ross Sea (-2.5-7.5^{o}C) (McKay et al., 2012a). Our overestimation of ocean temperatures is probably not due to an analytical error, given our close approximation of Mg/Ca in reference materials (Table 1), or calibration choice, because we calculate high temperatures in both species across multiple calibrations (Mawbey et al., 2020; Nürnberg, 1995; Elderfield and Ganssen, 2000; Kozdon et al., 2009). Our Holocene Mg/Ca values are ~1.0 mmol/mol for *Trifarina* and 0.82 mmol/mol for *N. pachyderma*, which are similar to Holocene Mg/Ca in *Trifarina* (Mawbey et al., 2020; Hillenbrand et al., 2017) and *N. pachyderma* (Hendry et al., 2009) from Antarctic margin sediment. However, because foraminifer Mg/Ca records from Antarctic shelves do not exist for the Plio-Pleistocene, we cannot use comparisons to determine how reasonable Mg/Ca values are downcore. To understand why Mg/Ca-temperatures are high in Ross Sea foraminifers during the Plio-Pleistocene, we consider potential influences on Mg/Ca that are alternative to temperature.

7.1.2 Dissolution and diagenetic influence: The primary stable isotope and Mg/Ca signal in foraminifers can be corrupted by dissolution in the water column or on the sediment surface when exposed to waters undersaturated with respect to $CaCO_3$ (Spero et al., 1997; Lorens et al., 1977; Brown and Elderfield, 1996; Regenberg et al., 2014; Lea, 2014). Dissolution enriches $\delta^{18}O$ and $\delta^{13}C$ via preferential removal of the lighter isotopes (Rosenthal et al., 2000; Dekens et al., 2002; Wu et al., 1990) and lowers foraminifer Mg/Ca (Brown and Elderfield, 1996). Hence, dissolution cannot explain high Ross Sea temperature. Instead, we consider the possibility that diagenesis influences stable isotope records.

U1523 foraminifer preservation varies between excellent to poor based on visual inspection via light microscopy. Excellent preservation is characterized by glassy and translucent tests, whereas dull, chalky, slightly pink, and perforated tests reflect poor preservation. We

selectively picked the best-preserved foraminifers, but true preservation is difficult to determine solely through light microscopy, and few foraminifers in some samples precluded selective picking. Samples with less foraminifers may reflect a shallow lysocline, and thus may have been deposited under relatively corrosive waters. Foraminifers are generally low throughout lithologic Unit II (3.1-2.2 Ma), with the exception of shell hashes at the base of the sequence (3.1 Ma) containing numerous juvenile *N. pachyderma*, likely reflecting penecontemporaneous reworking (McKay et al., 2019). In Unit I, we note few *Trifarina* and *N. pachyderma* in low MS intervals at 0.20 Ma and from 0.40 Ma to 0.30 Ma. Because $\delta^{18}O$ and $\delta^{13}C$ are generally depleted at these depths, the observed trends are probably not due to dissolution despite low foraminifer abundance. Large negative benthic foraminifer $\delta^{13}C$ excursions between ~41 and 30 m CCSF (2.4-2.0 Ma) are not accompanied by anomalous $\delta^{18}O$ values, and thus are likely not related to diagenetic alteration (Figure 7). We attribute these anomalously negative $\delta^{13}C$ values during the early Pleistocene to phytodetrital accumulation on the seafloor, which depletes the $\delta^{13}C_{DIC}$ of porewaters in which infaunal *Trifarina* calcifies (Grossman, 1984; Mackensen et al., 1993). This phytodetrital accumulation may reflect sluggish currents over U1523 during the early Pleistocene.

Although high Mg/Ca in U1523 foraminifers is likely to be at least partially influenced by contamination via diagenetic overgrowths and clays, we are reluctant to attribute diagenetic overgrowths as the principle driver of Mg/Ca due to our vigorous reductive cleaning protocol, the lack of covariance between *Trifarina* Mg/Ca, Mn/Ca, and the relatively weak correlation between *N. pachyderma* Mg/Ca and Mn/Ca compared to other Antarctic foraminifer studies (Figure 9) (Hillenbrand et al., 2017). Additionally, neither species Mg/Ca is correlated significantly correlated with Sr/Ca. Whereas we cannot exclude the possibility that U1523

foraminifer geochemical trends are influenced by diagenesis, there is evidence that the primary composition of the tests has been retained. Namely, fluctuations in Mg/Ca are visually correlated with $\delta^{13}C$, suggesting a similar mechanism driving both signals. Low $\delta^{13}C$ pairs with high Mg/Ca, which could reflect recrystallization in low $\delta^{13}C$ porewaters. However, intervals with low $\delta^{13}C$ and high Mg/Ca (notably around 0.40 Ma) are not accompanied by anomalous $\delta^{18}O$. If Mg/Ca is driven by temperature in *N. pachyderma*, a common environmental mechanism to explain the $\delta^{13}C$ and Mg/Ca covariance is warm mCDW, which imparts a light $\delta^{13}C$ signature on foraminifers (Shevenell and Kennett, 2002; Hillenbrand et al., 2017).

7.1.3 Mg/Ca secondary influences: Secular variations in Mg/Ca_{sw} cannot explain overestimated temperatures, because reconstructions of Plio-Pleistocene Mg/Ca_{sw} provide evidence for slightly smaller Mg/Ca_{sw} at 1.4 Ma relative to today (Evans et al., 2016), which would create a cold bias in mid-Pleistocene temperatures. High *N. pachyderma* Mg/Ca could reflect higher salinities due to less glacial meltwater influence, brine-rejection during sea-ice formation, and/or more mCDW influence at U1523. However, typical Mg/Ca-salinity sensitivity estimates are too low (~4-6%; Lea et al., 1999; Gray and Evans, 2019) to solely account for high Mg/Ca-temperatures. *N. pachyderma* (sinistral) have been found to live in brine channels of sea ice, which may complicate their use in ice-proximal Mg/Ca temperature reconstructions (Lipps and Krebs, 1974; Hendry et al., 2009) based on anomalously high Mg/Ca in *N. pachyderma* from sites covered by sea ice (Nürnberg, 1995; Meland et al., 2006; Kozdon et al., 2009; Vázquez Riveiros et al., 2016). Hendry et al. (2009) found that Mg/Ca-temperatures in *N. pachyderma* from the Antarctic peninsula are ~1^{o}C higher than expected during sea ice cover in austral winter, and attributed this result to elevated carbonate ion concentrations during at the ice-water interface. Whereas high Mg/Ca in Ross Sea *N. pachyderma* may partially reflect the influence of sea-ice cover, the

temperature deviation quantified in Hendry et al. (2009) is too small to account for temperatures that surpass 10°C. Furthermore, *Trifarina* Mg/Ca also produces overestimated temperatures, suggesting an influence on Mg/Ca beyond foraminiferal depth habitat. We ultimately exercise caution when interpreting Mg/Ca records by focusing on Mg/Ca trends rather than absolute temperatures.

7.2 Long-term Plio-Pleistocene Ross Sea temperature and ice volume changes: The upsection $\delta^{18}O$ increases of 1.3-1.4‰ reflects ice growth and cooling over the last 3.2 Ma. If 60% of this $\delta^{18}O$ increase is due to ice expansion (Lear et al., 2000), our $\delta^{18}O$ records imply a cooling of Ross Sea waters by 4°C (Shackleton, 1974). U1523 Mg/Ca records reveal a 4.4°C and 4.8°C cooling in deep and surface waters over the last 3.1 Ma, consistent with the $\delta^{18}O$-temperature estimate and Plio-Pleistocene cooling of 4°C estimated from deep sea Mg/Ca records (Billups and Schrag, 2002).

To isolate the ice volume signal from benthic $\delta^{18}O$, we calculated the $\delta^{18}O$ of seawater ($\delta^{18}O_{sw}$) using the paleotemperature equation by Shackleton (1974) and the Mg/Ca-temperature calibration of Elderfield et al. (2010): $\delta^{18}O_{sw} = (\delta^{18}O_{calcite} + 0.27) - 0.25 * (16.9 - ((Mg/Ca - 1)/0.1))$ (Figure 12). To assess meltwater input into the Ross Sea, we calculated planktic $\delta^{18}O_{sw}$ as per Mashiotta et al. (1999) with the temperature calibration of Vázquez Riveiros et al. (2016): $\delta^{18}O_{sw} = (\delta^{18}O_{calcite} + 0.27) - 4.38 - \sqrt{(4.38 - 4 * 0.1 * 16.9 - Temp) / (2 * 0.1)}$. Due to high Mg/Ca-temperatures, our $\delta^{18}O_{sw}$ values are higher than expected (LeGrande and Schmidt, 2006), and so we focus on trends rather than absolute values and sea level reconstructions. We aim to assess Antarctic ice sheet fluctuations during the Plio-Pleistocene with $\delta^{18}O_{sw}$ reconstructions. However, because $\delta^{18}O_{sw}$ contains a global ice volume signal, $\delta^{18}O_{sw}$ records are typically incapable of revealing Antarctica's specific contribution after bipolar glaciation at ~2.6 Ma. Our

ice-proximal $\delta^{18}O_{sw}$ records contain this global ice volume signal, but overprinting by local processes related to surface glacial meltwater and precipitation provides direct information on Antarctica ice fluctuations in the Ross embayment. These local hydrologic processes should have a greater influence on the $\delta^{18}O_{sw}$ in planktics relative to benthics. The correspondence between benthic and planktic $\delta^{18}O_{sw}$ trends suggests that both records can be used to assess Antarctic ice sheet variability (Figure 12).

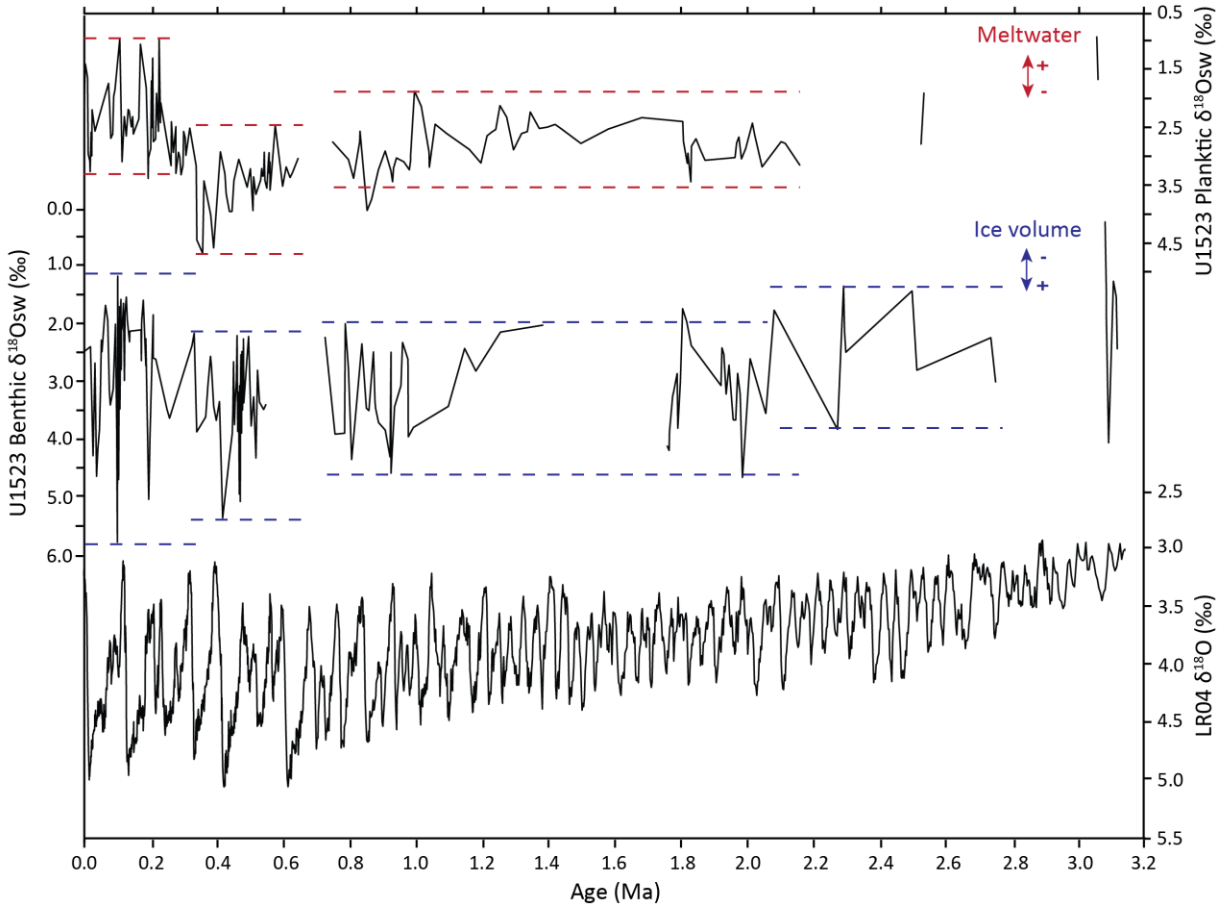

Figure 12: Antarctica's contribution to the global ice volume record over the last 3.2 Ma. Dashed lines highlight the 100 Kyr pacing of maxima $\delta^{18}O_{sw}$ indicative of ice growth during the late Pleistocene.

Our new benthic and planktic $\delta^{18}O_{sw}$ records show increasing ice volume since the late Pliocene (3.2 Ma) with step-like expansions at ~2.1 Ma and 0.8 Ma. This pattern of ice-growth is consistent with sediment from the AND-1B drill site, which document an increase in sea ice

duration and extent in the Ross embayment after ~2.6 Ma (Naish et al., 2009; McKay et al., 2012b) and ice expansion at the MPT (McKay et al., 2012b). Large clasts are visible in muds throughout the late Pliocene to middle Pleistocene U1523 sequence, but are not visible after 0.65 Ma, probably due to limited ice rafting under more stable ice conditions and ice shelves persisting through interglacials. Our new records corroborate hypotheses of Antarctic ice growth at the MPT based on ice-proximal foraminifer $\delta^{18}O$ from the Weddell Sea continental margin (Mackensen et al., 1994) and Prydz Bay trough mouth fan (Theissen et al., 2003), as well as modeling (Raymo et al., 2006) and deep-sea foraminifer records (Elderfield et al., 2012; Ford and Raymo, 2020). Ross Sea benthic $\delta^{18}O_{sw}$ peaks are spaced ~100 Kyr apart after the MPT, implying an eccentricity-modulation of Antarctic ice variations (Figure 12). This finding supports ice-proximal evidence of orbitally forced ice sheets during the Pliocene and early Pleistocene from AND-1B (Naish et al., 2009) and Site U1361 in the Wilkes Subglacial Basin (Patterson et al., 2014; Wilson et al., 2018). However, improvements in the U1523 chronology are necessary to validate this interpretation.

We attribute the mid-Pleistocene hiatus (0.75-0.65 Ma) to a strengthening of bottom currents on the outer Ross continental shelf. Glacial grounding lines did not reach U1523 during the Last Glacial Maximum, as indicated by the absence of megascale glacial lineations on the Iselin Bank (Anderson et al., 2002; Halberstadt et al., 2016), and seismic profiles of U1523 show no evidence of glacial erosion (McKay et al., 2019); thus, this unconformity is likely not the product of erosion from glacial overriding. Instead, we infer that the increase in benthic $\delta^{13}C$ after the hiatus indicates greater RSBW outflow (Figure 13). The concurrent $\delta^{18}O_{sw}$ increase may reflect enhanced sea-ice formation, which drives polynya-style mixing and dense bottom water production. Small gradients between benthic and planktic $\delta^{13}C$ and $\delta^{18}O$ from 0.60-0.20 Ma

lends support to an intensification of water column mixing after the MPT hiatus. Likewise, relatively high MS from 0.65 to 0.45 Ma is consistent with stronger bottom current strength, based on the fidelity between MS and grain size in U1523 sediment.

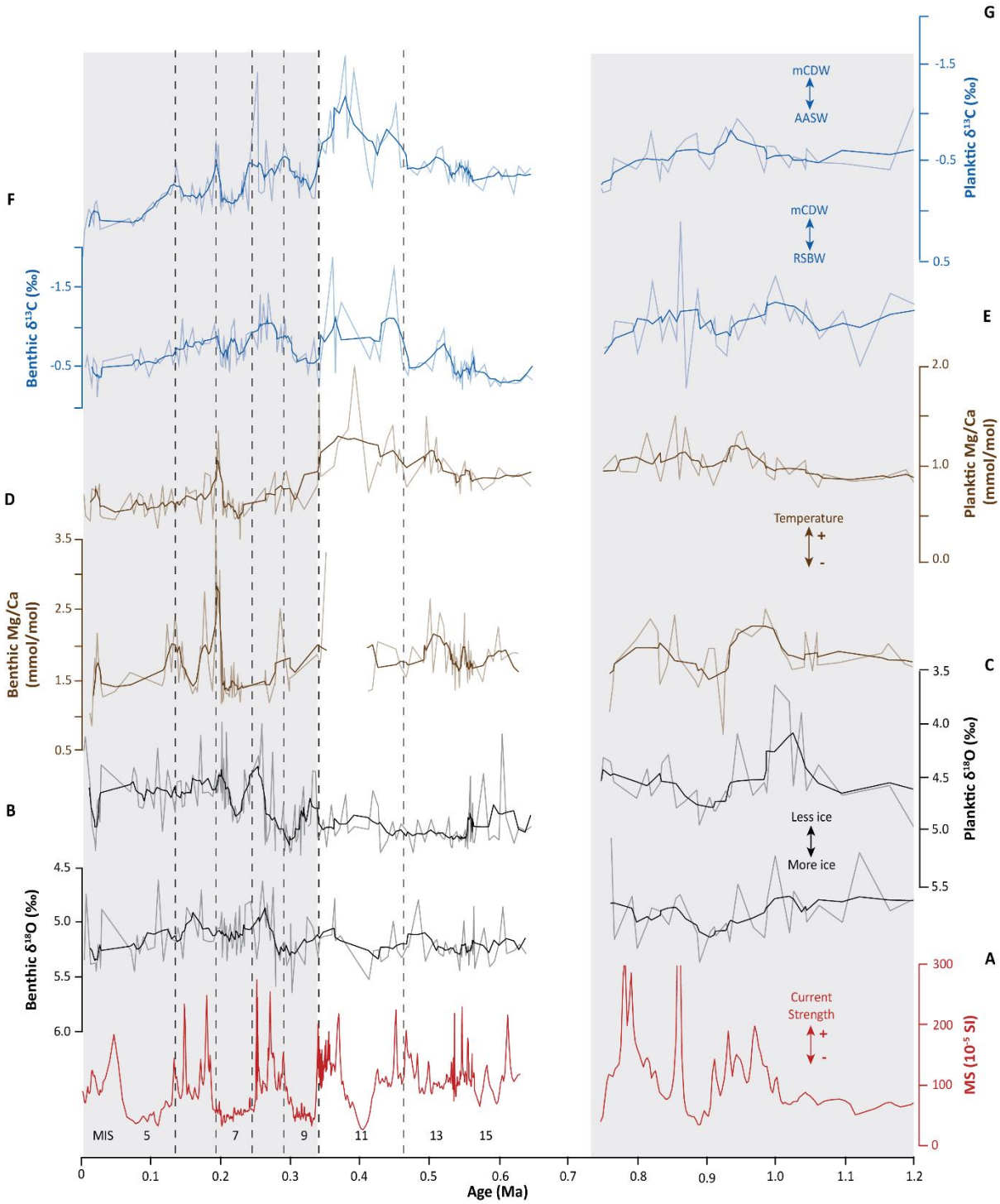

Figure 13: Paleoceanographic changes in the Ross Sea during the mid-late Pleistocene. From bottom to top: (A) Magnetic Susceptibility (MS), (B) benthic *Trifarina* and (C) planktic *N. pachyderma* $\delta^{18}O$, (D) benthic and (E) planktic Mg/Ca, and (F) benthic and (G) planktic $\delta^{13}C$. Solid lines are 5-point running averages for (C) to (H). Vertical dashed lines trace intervals with relatively light $\delta^{13}C$, which we attribute to a greater mCDW presence on the Ross Shelf. Interglacial Marine Isotope Stages (MIS) tied to low MS intervals (Figure 6) are numbered on (A). Vertical grey bars delineate pre (1.2-0.75 Ma) and post (0.65-0.35 Ma) mid-Pleistocene transition, where the pacing of glacial/interglacial cycles switches from 100 Kyr to 40 Kyr durations, and post mid-Brunhes Event (last 0.35 Ma) which marks an increase in the amplitude of glacial/interglacial fluctuations.

The magnitude of Ross Sea benthic $\delta^{18}O_{sw}$ fluctuations increases at 0.30 Ma. This shift is indicative of the mid-Brunhes Event, which is characterized by a change in the amplitude of glacial and interglacial cycles between MIS 13 and 11 (~0.43 Ma) in stacked benthic $\delta^{18}O$ records (Lisiecki and Raymo, 2005). The apparent mid-Brunhes transition in Ross Sea benthic $\delta^{18}O_{sw}$ occurs after MIS 10, and due to uncertainties in our age model, it is unclear if this offset implies a delayed reaction of Antarctica's ice sheets or an issue with the U1523 chronology. Extended MS sequences after MIS 11 in U1523 sediment suggests a transition to more prolonged and distinct glacial and interglacial cycles in the Ross Sea after the mid-Brunhes Event. Alternatively, high MS intervals could reflect periodic strengthening of currents during climate transitions, rather than full glacial and interglacial periods.

7.3 Late Pleistocene mCDW presence on the Ross outer shelf: The close correspondence between planktic $\delta^{13}C$ minima (dashed lines in Figure 13) and Mg/Ca maxima indicates intervals of enhanced warmth and nutrient-rich mCDW presence on the Ross shelf edge during the late Pleistocene (last 1.2 Ma). The present-day Ross Sea continental shelf is considered a cold shelf with limited mCDW-driven melting due to a strong ASC (Thompson et al., 2018; Adusumilli et al., 2020). We propose that low $\delta^{13}C$ and high Mg/Ca reflect intervals of stronger mCDW influence on U1523, potentially due to a weaker ASC. Our records provide evidence for a

distinct and prolonged warm excursion during MIS 10 to 12 (Figure 13). Assignment of this warm interval to MIS 11 is supported by peak radiogenic Nd isotopes (Wilson et al., 2018) and ^{234}U enrichment (Blackburn et al., 2020) in sediments from the Wilkes Subglacial Basin during MIS 11, which show prominent warmth and East Antarctic Ice Sheet retreat. Following MIS 10, low $\delta^{13}C$ and warm Mg/Ca occur at the top and base of two high MS intervals that we assign to MIS 6 and 8. Within these high MS intervals, low $\delta^{18}O$ indicates reduced ice volume and/or meltwater influence concurrent with mCDW presence. This evidence of ice loss in high MS sediment contrasts our interpretation that coarse-grained intervals reflect periods of glacial advance. When constructing the late Pleistocene U1523 chronology, we hypothesized that coarse sediment reflects winnowing of fines by strong bottom currents under enhanced glacial Southern Hemisphere westerlies (Martínez-Garcia et al., 2011), and/or that ice-proximal glaciomarine sedimentation provides coarse material to U1523 (McKay et al., 2019). Our late Pleistocene $\delta^{18}O$ records indicates that sand and diamict facies may instead be the product of winnowing via stronger currents. We propose that stronger currents drive enhanced CDW upwelling onto the Ross shelf during the late Pleistocene (last 0.35 Ma), evident by low $\delta^{13}C$ and high Mg/Ca, which led to ice loss that imparted a light $\delta^{18}O$ signature on foraminifers concentrated in coarse grained intervals.

8 Conclusions

We present the first Plio-Pleistocene (last 3.1 Ma) benthic and planktic foraminifer $\delta^{18}O$, $\delta^{13}C$, and Mg/Ca records from Antarctic margin sediment at IODP Site U1523. Benthic and planktic $\delta^{18}O$ reveal an upsection increase of 1.4-1.5‰, reflecting ice growth and Ross Sea cooling of ~4^{o}C during the late Pliocene to Pleistocene, consistent with deep-sea records of a ~1.7‰ $\delta^{18}O$ increase (Lisiecki and Raymo, 2005). The consistency between the global and Ross Sea foraminifer signal confirms the utility of Ross continental shelf foraminifer $CaCO_3$ for reconstructions of past paleoenvironmental conditions. Our $\delta^{18}O_{sw}$ records support an increase in Antarctic ice volume and current strength at the mid Pleistocene Transition (MPT). We attribute an increase in benthic foraminifer $\delta^{13}C$ after the MPT to enhanced deep water ventilation, perhaps due to increased Ross Sea Bottom Water production driven by an increase in sea ice formation and polynya-style mixing. Our records demonstrate a covariance between low $\delta^{18}O$, $\delta^{13}C$, and high Mg/Ca during the late Pleistocene, which indicates ice sheet sensitivity during intervals of greater modified Circumpolar Deep Water presence on the Ross shelf. One such interval with a striking high Mg/Ca and low $\delta^{13}C$ perturbation appear to be MIS 11, though age model uncertainties limit our determination of this event's timing. To determine Antarctic ice-ocean interactions during super interglacials like MIS 11, we require an improved U1523 chronology and direct records of ice sheet stability from provenance and/or lithofacies assessments.

References

Adusumilli, S., Fricker, H.A., Medley, B., Padman, L., and Siegfried, M.R., 2020. Interannual variations in meltwater input to the Southern Ocean from Antarctic ice shelves. Nature Geoscience, 13, 616-620.

Ainley, D.G, and Jacobs, S.S., 1981. Sea-bird affinities for ocean and ice boundaries in the Antarctic. Deep-Sea Research, 28 (10), 1173-1185.

Alonso, B., Anderson, J.B., Díaz, J.I., and Bartek, L.R., 1992. Pliocene-Pleistocene seismic stratigraphy of the Ross Sea: Evidence for multiple ice sheet grounding episodes. Contributions to Antarctic Research III, Antarctic Research Series, 57, 93-103.

Anderson, J.B., Shipp, S.S., Lowe, A.L., Wellner, J.S., and Mosola, A.B., 2002. The Antarctic Ice Sheet during the Last Glacial Maximum and its subsequent retreat history: a review. Quaternary Science Reviews, 21 (1-3), 49-70.

Arbuszewski, J., deMenocal, P., Kaplan, A., and Christa Farmer, E., 2010. On the fidelity of shell-derived δ18Oseawater estimates. Earth and Planetary Science, 300 (3-4), 185-196.

Barker, S., Greaves, M., and Elderfield, H., 2003. A study of cleaning procedures used for foraminiferal Mg/Ca paleothermometry. Geochemistry, Geophysics, Geosystems, 14 (9), 1-20.

Bauch, D., Carstens, J., and Wefer, G., 1997. Oxygen isotope composition of living *Neogloboquadrina pachyderma* (sin.) in the Arctic Ocean. Earth and Planetary Letters, 146 (1-2), 47-58.

Bé, A.W.H., and Tolderlund, D.S., 1971. Distribution and ecology of living planktonic foraminifera in surface waters of the Atlantic and Indian Oceans. Micropaleontology of the Oceans, Cambridge University Press, London, 105-149.

Beltran, C., Golledge, N.R., Ohneiser, C., Kowalewskie, D.E., Sicre, M.A., et al., 2020. Southern Ocean temperature records and ice-sheet models demonstrate rapid Antarctic ice sheet retreat under low atmospheric CO2 during Marine Isotope Stage 31. Quaternary Science Reviews, 228, 106069.

Bergamasco, A., Defendi, V., Zambianchi, E., and Spezie, G., 2002. Evidence of dense water overflow on the Ross Sea shelf-break. Antarctic Science, 14 (3), 271–277.

Bertram, R.A., Wilson, D.J., van de Flierdt, T., McKay, R.M., Patterson, M.O., Jimenez-Espejo, F.J., et al., 2018. Pliocene deglacial event timelines and the biogeochemical response

offshore Wilkes Subglacial Basin, East Antarctica. Earth and Planetary Science Letters, 484, 109-116.

Billups, K., and Schrag, D.P., 2002. Paleotemperature and ice volume of the past 27 Myr revisited with paired Mg/Ca and $^{18}O/^{16}O$ measurements on benthic foraminifera. Paleoceanography, 17 (1), 3-1-3-11.

Blackburn, T., Edwards, G.H., Tulaczyk, S., Scudder, M., Piccione, G., Hallet, B., et al., 2020. Ice retreat in Wilkes Basin of East Antarctica during a warm interglacial. Nature, 583, 554–559.

Bohaty, S.M., Zachos, J.C., and Delaney, M.L., 2012. Foraminiferal Mg/Ca evidence for Southern Ocean cooling across the Eocene–Oligocene transition. Earth and Planetary Science Letters, 317–318, 251-261.

Boyle, E.A., 1983. Manganese carbonate overgrowths on formainifera tests. Geochimica et Cosmochimica Acta, 47, 1815–1819.

Boyle, E. A. and Keigwin, L. D., 1985/86. Comparison of Atlantic and Pacific paleochemical records for the last 215,000 years: Changes in deep ocean circulation and chemical inventories. Earth and Planetary Science Letters, 76, 135-150.

Brown, S.J., and Elderfield, H., 1996. Variations in Mg/Ca and Sr/Ca ratios of planktonic foraminifera caused by postdepositional dissolution: evidence of shallow Mg-dependent dissolution. Paleoceanography, 11, 543–551.

Camerlenghi, A., Rebesco, M., and Pudsey, C.J., 1997. High resolution terrigenous sedimentary record of a sediment drift on the Antarctic Peninsula Pacific margin (initial results of the 'SEDANO' Program). The Antarctic Region: Geological Evolution and Processes, 705-710.

Carmack, E., 1977. Water characteristics of the Southern Ocean south of the Polar Front, in A Voyage of Discovery: G. Deacon 70th Anniversary Volume, edited by M. Angel, Deep Sea Research, 24, 15–42.

Conte, R., Rebesco, M., De Santis, L., Colleoni, F., Bensi, M., et al., submitted. Bottom current control on sediment deposition between the Iselin Bank and the Hillary Canyon (Antarctica) since the late Miocene: an integrated seismic-oceanographic approach. Deep Sea Research Part I.

Cook, C.P., van de Flierdt, T., Williams, T., Hemming, S.R., Iwai, M., et al., 2013. Dynamic behaviour of the East Antarctic ice sheet during Pliocene warmth. Nature Geoscience, 6, 765-769.

Cook, A.J., Holland P.R., Meredith, M.P., Murray, T., Luckman, A., and Vaughan, D.G., 2016. Ocean forcing of glacier retreat in the western Antarctic Peninsula. Science, 353 (6296), 283-286.

Coxall, H.K., Wilson, P.A., Pälike, H., Lear, C.H., and Backman, J., 2005. Rapid stepwise onset of Antarctic glaciation and deeper calcite compensation in the Pacific Ocean. Nature, 433, 53–57.

Cramer, B.S., Toggweiler, J.R., Wright, J.D., Katz, M.E., and Miller, K.G., 2009. Ocean overturning since the Late Cretaceous: Inferences from a new benthic foraminiferal isotope compilation. Paleoceanography, 24, PA4216.

de Villiers, S., Greaves, M., and Elderfield, H., 2002. An intensity ratio calibration method for the accurate determination of Mg/Ca and Sr/Ca of marine carbonates by ICP-AES. Geochemistry, Geophysics, Geosystems, 3, 623-634.

DeConto, R.M., and Pollard, D., 2016. Contribution of Antarctica to past and future sea-level rise. Nature, 531, 591–597.

DeConto, R.M., Pollard, D., and Kowalewski, D., 2012. Modeling Antarctic ice sheet and climate variations during Marine Isotope Stage 31. Global and Planetary Change, 88–89, 45–52.

DeJong, H.B., Dunbar, R.B., Mucciarone, D., and Koweek, D.A., 2015. Carbonate saturation state of surface waters in the Ross Sea and Southern Ocean: controls and implications for the onset of aragonite undersaturation. Biogeosciences, 12, 6881–6896.

Dekens, P.S., Lea, D.W., Pak, D.K., and Spero, H.J., 2002. Core top calibration of Mg/Ca in tropical foraminifera: Refining paleo-temperature estimation. Geochemistry, Geophysics, Geosystems, 3 (1022), 1-29.

Dinniman, M.S., Klinck, J.M., and Smith, W.O., 2011. A model study of Circumpolar Deep Water on the West Antarctic Peninsula and Ross Sea continental shelves. Deep-Sea Research II, 58, 1508–1523.

Elderfield, H., and Gansse, G., 2000. Past temperature and $\delta^{18}O$ of surface ocean waters inferred from foraminiferal Mg/Ca ratios. Nature, 405, 442-445.

Elderfield, H., Vautravers, M., and Cooper, M., 2002. The relationship between shell size and Mg/Ca, Sr/Ca, $\delta^{18}O$, and $\delta^{13}C$ of species of planktonic foraminifera. Geochemistry, Geophysics, Geosystems, 3 (8), 1-13.

Elderfield, H., Yu, J., Anand, P., Kiefer, T., and Nyland, B., 2006. Calibrations for benthic foraminiferal Mg/Ca paleothermometry and the carbonate ion hypothesis. Earth and Planetary Science Letters, 250, 633-649.

Elderfield, H., Greaves, M., Barker, S, Hall, I. R., Tripati, A., et al., 2010. A record of bottom water temperature and seawater $\delta^{18}O$ for the Southern Ocean over the past 440 Kyr based on Mg/Ca of benthic foraminiferal *Uvigerina spp.* Quaternary Science Reviews, 29 (1-2), 160-169.

Elderfield, H., Ferretti, P., Greaves, M., Crowhurst, S., McCave, I.N., Hodell, D., Piotrowski, A. M., 2012. Evolution of Ocean Temperature and Ice Volume Through the Mid-Pleistocene Climate Transition. Science, 337 (6095), 704-709.

Escutia, C., Bárcena, Lucchi, R.G., Romero, O., Ballengeer, A.M., Gonzalez, J.J., and Harwood, D.M., 2009. Circum-Antarctic warming events between 4 and 3.5 Ma recorded in marine sediments from the Prydz Bay (ODP Leg 188) and the Antarctic Peninsula (ODP Leg 178) margins. Global Planetary Change, 69, 170-184.

Escutia, C., DeConto, R.M., Dunbar, R., De Santis, L., Shevenell, A., and Naish, T., 2019. Keeping an eye on Antarctic Ice Sheet stability. Oceanography, 32 (1), 32–46.

Evans, D., Brierley, C., Raymo, M.E., Erez, J., and Müller, W., 2016. Planktic foraminifera shell chemistry response to seawater chemistry: Pliocene-Pleistocene seawater Mg/Ca, temperature, and sea level change. Earth and Planetary Science Letters, 438, 139-148.

Feely, R.A., Doney, S.C., and Cooley, S.R., 2009. Ocean Acidification Present Conditions and Future Changes in a High-CO_2 World. Oceanography, 22 (4), 36-47.

Fillon, R.H., 1974. Late Cenozoic foraminiferal paleoecology of the Ross Sea, Antarctica. Micropaleontology, 20 (2), 129-150.

Flower, B.P., and Kennett, J.P., 1994. The middle Miocene climatic transition: East Antarctic ice sheet development, deep ocean circulation and global carbon cycling. Palaeogeography, Palaeoclimatology, Palaeoceology, 108, 537-555.

Ford, H.L., and Raymo, M.E., 2020. Regional and global signals in seawater $\delta^{18}O$ records across the mid-Pleistocene transition. Geology, 48 (2), 113–117.

Gill, A.E., 1973. Circulation and bottom water production in the Weddell Sea. Deep Sea Research, 20, 111-140.

Golledge, N. R., Kowalewski, D.E., Naish, T.R., Levy, R.H., Fogwill, C.J., and Gasson, E.G.W., 2015. The multi-millennial Antarctic commitment to future sea-level rise. Nature, 526, 421–425.

Gordon, A.L., Zambianchi, E., Orsi, A., Visbeck, M., Giulivi, C.F., Whitworth, T., and Spezie, G., 2004. Energetic plumes over the western Ross Sea continental slope. Geophysical Research Letters, 31, L21302.

Gordon, A.L., Orsi, A.H., Muench, R., Huber, B.A., Zambianchi, E., and Visbeck, M., 2009. Western Ross Sea continental slope gravity currents. Deep-Sea Research II, 56, 796–817.

Gray, W.R., and Evans, D., 2019. Nonthermal Influences on Mg/Ca in Planktonic Foraminifera: A Review of Culture Studies and Application to the Last Glacial Maximum. Paleoceanography and Paleoclimatology, 34 (3), 306-315.

Greaves, M., Caillon, N., Rebaubier, H., Bartoli, G., Bohaty, S., et al., 2008. Interlaboratory comparison study of calibration standards for foraminiferal Mg/Ca thermometry. Geochemistry, Geophysics, Geosystems, 9 (8), Q08010.

Grobe, H., Mackensen, A., Hubberten, H.-W., Spiess, V., and Fütterer, 1990. Stable isotope and late Quaternary sedimentation rates at the Antarctic continental margin. U. Bleil and J. Thiede (eds.). Geological History of the Polar Oceans: Arctic versus Antarctic. Kluwer Academic Publishers, Netherlands, 539-572.

Grossman, E.L., 1984. Carbon isotopic fractionation in live benthic foraminifera—comparison with inorganic precipitate studies. Geochimica et Cosmochimica Acta, 48 (7), 1505-1512.

Gudmundsson, G.H., Paolo, F.S., Adusumilli, S., and Fricker, H.A., 2019. Instantaneous Antarctic ice-sheet mass loss driven by thinning ice shelves. Geophysical Research Letters, 46, 13903–13909.

Halberstadt, A.R.W., Simkins, L.M., Greenwood, S.L., and Anderson, J.B., 2016. Past ice-sheet behaviour: retreat scenarios and changing controls in the Ross Sea, Antarctica. The Cryosphere, 10, 1003–1020.

Haug, G.H., and Tiedemann, R., 1998. Effect of the formation of the Isthmus of Panama on Atlantic Ocean thermohaline circulation. Nature, 393, 673-676.

Hayes, D.E., and Frakes, L.D., 1975. General synthesis, deep sea drilling project Leg 28, Initial Reports of the Deep Sea Drilling Project, 28, U.S. Gov. Print. Off, Washington, D.C, 919-942.

Hendry, K.R., Rickaby, R.E.M., Meredith, M.P., and Elderfield, H., 2009. Controls on stable isotope and trace metal uptake in *Neogloboquadrina pachyderma (*sinistral) from an Antarctic sea-ice environment. Earth and Planetary Science Letters, 278 (1), 67-77.

Hepp, D.A., Mörz, T., and Grützner, J., 2006. Pliocene glacial cyclicity in a deep-sea sediment drift (Antarctic Peninsula Pacific Margin). Palaeogeography, Palaeoclimatology, Palaeoecology, 231 (1-2), 181-198.

Hillenbrand, C.D., Kuhn, G., and Frederichs, T., 2009. Record of a Mid-Pleistocene depositional anomaly in West Antarctic continental margin sediments: an indicator for ice-sheet collapse?. Quaternary Science Reviews, 28, 1147-1159.

Hillenbrand, C.D., Smith, J.A., Hodell, D.A., Greaves, M., Poole, C.R., et al., 2017. West Antarctic Ice Sheet retreat driven by Holocene warm water incursions. Nature, 547, 43-48.

Hönisch, B., Allen, K.A., Lea, D.W., Spero, H.J., Eggins, S.M., et al., 2013.The influence of salinity on Mg/Ca in planktic foraminifers – Evidence from cultures, core-top sediments and complementary $\delta^{18}O$. Geochimica et Cosmochimica Acta, 121, 196–213.

IODP-MI, 2011. IODP Depth Scale Terminology version 2.0. https://www.iodp.org/policies-and-guidelines/142-iodp-depth-scales-terminology-april-2011/file

Jacobs, S.S., 1991. On the nature and significance of the Antarctic Slope Front. Marine Chemistry, 35 (1-4), 9-24.

Jacobs, S.S., Giulivi, C.F., and Mele, P.A., 2002. Freshening of the Ross Sea during the Late 20th Century. Science, 297 (5580), 386-389.

Jimenez-Espejo, F.L., Presti, M., Kuhn, G., Mckay, R., Crosta, X., et al., 2020. Late Pleistocene oceanographic and depositional variations along the Wilkes Land margin (East Antarctica) reconstructed with geochemical proxies in deep-sea sediments. Global and Planetary Change, 184, 103045.

Jouzel, J., Masson-Delmotte, V., Cattani, O., Dreyfus, G., Falourd, S., et al., 2007. Orbital and millennial Antarctic climate variability over the past 800,000 years. Science, 317 (5839), 793-796.

Kennett, J.P., 1966. Foraminiferal evidence of a shallow calcium carbonate solution boundary, Ross Sea, Antarctica. Science, 153, 191-193.

Kennett, J.P., 1968. The fauna of the Ross Sea, Part 6: ecology and distribution of foraminifera. New Zealand Department of Scientific and Industrial Research. Bulletin 186, 1-47.

Kennett, J.P., 1977. Cenozoic evolution of Antarctic glaciation, the circum-Antarctic Ocean, and their impact on global paleoceanography. Journal of Geophysical Research, 82 (27), 3843-3860.

Kim, K., Lee, I. J., McKay, R.M., Yoo, K.C., Bak, Y.S., et al., 2020. Late Pleistocene paleoceanographic changes in the Ross Sea – Glacial-interglacial variations in paleoproductivity, nutrient utilization, and deep-water formation. Quaternary Science Reviews, 239 (106356), 1-11.

King, T.M., Rosenheim, B.E., Post, A.L., Gabris, T., Burt, T., and Domack, E.W., 2018. Large-scale intrusion of Circumpolar Deep Water on Antarctic margin recorded by stylasterid corals. Paleoceanography and Paleoclimatology, 33, 1306–1321.

Kohfeld, K.E., Fairbanks, R.G., Smith, S.L., and Walsh, I.D., 1996. *Neogloboquadrina pachyderma* (sinistral coiling) as paleoceanographic tracers in polar oceans: Evidence from northeast water polynya plankton tows, sediment traps, and surface sediments. Paleoceanography and Paleoclimatology, 11 (6), 679-699.

Kozdon, R., Eisenhauer, A., Weinelt, M., Meland, M.Y., and Nürnberg, D., 2009. Reassessing Mg/Ca temperature calibrations of *Neogloboquadrina pachyderma* (sinistral) using paired $\delta^{44/40}$Ca and Mg/Ca measurements. Geochemistry, Geophysics, Geosystems, 10 (3), 1-14.

Kroopnick, P.M., 1974. The dissolved O_2, CO_2,^{13}C system in the eastern equatorial Pacific. Deep-Sea Research, 21, 211-227.

Lea, D.W., 1999. Trace elements in foraminiferal calcite. In: B. K. Sen Gupta (Ed.), Modern foraminifera. Dordrecht: Kluwer. 259–280.

Lea, D.W., 2014. Elemental and isotopic proxies of past ocean temperatures. In: Holland H.D. and Turekian K.K. (eds.) Treatise on Geochemistry, Second Edition (8), 373-397.

Lear, C.H., Elderfield, H., and Wilson, P.A., 2000. Cenozoic deep-sea temperatures and global ice volumes from Mg/Ca in benthic foraminiferal calcite. Science, 287, 269–272.

Lear, C.H., Rosenthal, Y., and Slowey, N., 2002. Benthic foraminiferal Mg/Ca-paleothermometry: A revised core-top calibration. Geochimica et Cosmochimica Acta, 66 (19), 3375-3387.

Lear, C.H., Mawbey, E.M., and Rosenthal, Y., 2010. Cenozoic benthic foraminiferal Mg/Ca and Li/Ca records: Toward unlocking temperatures and saturation states. Paleoceanography, 25, PA4215.

LeGrande, A.N., and Schmidt, G.A., 2006. Global gridded data set of the oxygen isotopic composition in seawater. Geophysical. Research Letters, 33, L12604

Lide, D.R., 2007. CRC Handbook of Chemistry and Physics 88th Edition 2007-2008. CRC Press, Taylor & Francis, Boca Raton, FL, 4-78.

Lipps, J.H., and Krebs, W.N., 1974. Planktonic foraminifera associate with Antarctic sea-ice. Journal of Foraminiferal Research 4, 80-85.

Lisiecki, L.E., and Raymo, M.E., 2005. A Pliocene-Pleistocene stack of 57 globally distributed benthic δ^{18}O records. Paleoceanography, 20 (PA1003).

López-Quirós, A., Escutia, C., Sánchez-Navas, A., Nieto, F., Garcia-Casco, A., et al., 2019. Glaucony authigenesis, maturity and alteration in the Weddell Sea: An indicator of paleoenvironmental conditions before the onset of Antarctic glaciation. Scientific Reports, 9, 13580.

Lorens, R.B., Williams, D.F., and Bender, M.L., 1977. The early nonstructural chemical diagenesis of foraminiferal calcite. Journal of Sedimentary Petrology, 47, 1602-1609.

Mackensen, A., Hubberten, H.-W., Bickert, T., Fischer, G., and Futterer, D.K., 1993. The $\delta^{13}C$ in benthic foraminiferal tests of *Fontbotia wuellerstorfi* (Schwager) relative to the $\delta^{13}C$ of dissolved inorganic carbon in Southern Ocean Deep Water: Implications for glacial ocean circulation models. Paleoceanography and Paleoclimatology, 8 (5), 587-610.

Mackensen, A., Grobe, H., Hubberten, H.-W., and Kuhn, G., 1994. Benthic foraminiferal assemblages and d13C-signal in the Atlantic sector of the Southern Ocean: glacial-to-interglacial contrasts. R. Zahn, T.F. Pederson, M.A. Kaminiski, and L. Labeyrie (Eds.), Carbon Cycling in the Glacial Ocean: Constraints on the Ocean's Role in Global Change, Springer-Verlag, Berlin, 105-144.

Mackensen, A., and Schmiedl, G., 2019. Stable carbon isotopes in paleoceanography: atmosphere, oceans, and sediments. Earth-Science Reviews, 197, 102893.

Marchitto, T.M., 2006. Precise multielemental ratios in small foraminifera samples determined by sector field ICP-MS. Geochemistry, Geophysics, Geosystems, 7 (5), 1-10.

Marshall, G.J., 2003. Trends in the Southern Annular Mode from Observations and Reanalyses. Journal of Climate, 16, 4134-4143.

Martin, P. A. and Lea, D. W., 2002. A simple evaluation of cleaning procedures on fossil benthic foraminiferal Mg/Ca. Geochemistry, Geophysics, Geosystems, 3 (10), 1-8.

Martínez-Garcia, A., Rosell-Melé, A, Jaccard, S.L., Geibert, W., Sigman, D.M., and Haug, G.H., 2011. Southern Ocean dust-climate coupling over the past four million years. Nature, 476, 312–315.

Mashiotta, T.A., Lea, D.W., and Spero, H.J., 1999. Glacial-interglacial changes in Subantarctic sea surface temperature and $\delta^{18}O$-water using foraminiferal Mg. Earth and Planetary Science Letters, 170, 417-432.

Mawbey, E., Hendry, K., Greaves, M., Hillenbrand, C.D., Kuhn, G., et al., 2020. Mg/Ca-Temperature Calibration for Polar Benthic foraminiferal species for reconstruction of bottom water temperatures in the Antarctic shelf regions. Geochimica et Cosmochimica Acta, 283, 54-66.

McKay, R., Naish, T., Carter, L., Riesselman, C., Dunbar, R., et al., 2012a. Antarctic and Southern Ocean influences on Late Pliocene global cooling. Proceedings of the National Academy of Sciences, 109 (17), 6423-6428.

McKay, R., Naish, T., Powell, R., Barrett, P., Scherer, R., et al., 2012b. Pleistocene variability of Antarctic Ice Sheet extent in the Ross embayment. Quaternary Science Reviews, 34, 93-112.

McKay, R.M., De Santis, L., Kulhanek, D.K., and the Expedition 374 Scientists, 2019. Proceedings of the International Ocean Discovery Program Volume 374 Ross Sea West Antarctic Ice Sheet History.

Meland, M.Y., Jansen, E., Elderfield, H., Dokken, T.M., Olsen, A., and Bellerby, R.G.J., 2006. Mg/Ca ratios in the planktonic foraminifer *Neogloboquadrina pachyderma* (sinistral) in the northern North Atlantic/Nordic Seas. Geochemistry, Geophysics, Geosystems, 7 (6), 1-18.

Miller, K.G., Wright, J.D., and Fairbanks, R.G., 1991. Unlocking the ice house: Oligocene-Miocene oxygen isotopes, eustasy, and margin erosion. Journal of Geophysical Research: Solid Earth, 96 (B4), 6829-6848.

Morrison, A.K., Hogg, A.M., England, M.H., and Spence, P., 2020. Warm Circumpolar Deep Water transport toward Antarctica driven by local dense water export in canyons. Science Advances, 6 (18), 1-9.

Mudelsee, M., and Schulz, M., 1997. The Mid-Pleistocene climate transition: onset of 100 ka cycle lags ice volume build-up by 280 ka. Earth and Planetary Science Letters, 151, 117-123.

Naish, T., Powell, R., Levy, R., Wilson, G., Scherer, R., et al., 2009. Obliquity-paced Pliocene West Antarctic ice sheet oscillations. Nature, 458 (7236), 322–328.

Nürnberg, D., 1995. Magnesium in tests of *Neogloboquadrina pachyderma* sinistral from high northern and southern latitudes. The Journal of Foraminiferal Research, 25 (4), 350–368.

Nyland, B.F., Jansen, E., Elderfield, H., and Andersson, C., 2006. *Neogloboquadrina pachyderma* (dex.) Mg/Ca and $\delta^{18}O$ records from the Norwegian Sea. Geochemistry, Geophysics, Geosystems, 7 (10), 1-18.

Odin, G.S., 1988. Green Marine Clays. Develop Sediment 45, Elsevier.

Osterman, L.E., and Kellogg, T.B., 1979. Recent benthic foraminiferal distributions from the Ross Sea, Antarctica: relation to ecologic and oceanographic conditions. Journal of Foraminiferal Research, 9 (3), 250-269.

Orsi, A.H., Whitworth, T., and Nowlin, W.D., 1995. On the meridional extent and fronts of the Antarctic Circumpolar Current. Deep Sea Research Part I: Oceanographic Research Papers, 42 (5), 641-673.

Orsi, A.H., Johnson, G.C., and Bullister, J.L., 1999. Circulation, mixing, and production of Antarctic Bottom Water. Progress in Oceanography, 43 (1), 55-109.

Orsi, A.H., and Wiederwohl, C.L., 2009. A recount of Ross Sea waters. Deep-Sea Research II 56, 778-795.

Patterson, M.O., McKay, R., Naish, T., Escutia, C., Jimenez-Espejo, F.J., et al., 2014. Orbital forcing of the East Antarctic ice sheet during the Pliocene and Early Pleistocene. Nature Geoscience, 7, 841-846.

Pena, L.D., Calvo, E., Cacho, I., Eggins, S., and Pelejero, C., 2005. Identification and removal of Mn-Mg-rich contaminant phases on foraminiferal tests: implications for Mg/Ca past temperature reconstructions. Geochemistry, Geophysics, Geosystems, 6 (9), 1-25.

Pollard, D., and DeConto, R.M., 2009. Modelling West Antarctic ice sheet growth and collapse through the past five million years. Nature, 458, 329-332.

Pritchard, H.D., Ligtenberg, S.R.M., Fricker, H.A., Vaughan, D.G., van den Broeke, M.R., and Padman, L., 2012. Antarctic ice-sheet loss driven by basal melting of ice shelves. Nature, 484, 502-505.

Prothro, L.O., Simkins, L.M., Majewski, W., and Anderson, J.B., 2018. Glacial retreat patterns and processes determined from integrated sedimentology and geomorphology records. Marine Geology, 395, 104-119.

Raymo, M.E., Lisiecki, L.E., and Nisancioglu, K.H., 2006. Plio-Pleistocene ice volume, Antarctic climate, and the global $\delta^{18}O$ record. Science, 313 (5786), 492–495.

Ravelo, A.C., Andreasen, D.H., Lyle, M., Olivarez Lyle A., and Wara, M.W., 2004. Regional climate shifts caused by a decline in atmospheric CO_2 levels. Nature, 454, 1102-1105.

Ravelo, A.C., and Hillaire-Marcel, C., 2007. The Use of Oxygen and Carbon Isotopes of Foraminifera in Paleoceanography in Developments in Marine Geology, Volume 1, Proxies in Late Cenozoic Paleoceanography, edited by C. Hillaire-Marcel and A. de Vernal, Elsevier, New York, 735-764.

Regenberg, M., Regenber, A., Garbe-Schönberg, D., and Lea, D.W., 2014. Global dissolution effects on planktonic foraminiferal Mg/Ca ratios controlled by the calcite-saturation state of bottom waters. Paleoceanography and Paleoclimatology, 29 (3), 127-142.

Rignot, E., and Jacobs, S.S., 2002. Rapid bottom melting widespread near Antarctic ice sheet grounding lines. Science, 296, 2020-2023.

Rignot, E., Jacobs, S., Mouginot, J., and Scheuchl, B., 2013. Ice-Shelf melting around Antarctica. Science, 341, 266-270.

Rignot, E, Mouginot, J., Scheuchla, B., van den Broeked, M., van Wessemd, M.J., and Morlighema, M., 2019. Four decades of Antarctic Ice Sheet mass balance from 1979–2017. Proceedings of the National Academy of Sciences, 116 (4), 1095–1103.

Rosenthal, Y., Field, P.M., and Sherrell, R.M., 1999. Precise determination of element/calcium ratios in calcareous samples using sector field inductively coupled plasma mass spectrometry. Anal. Chem., 71, 3248-3253.

Rosenthal, Y., Lohmann, G.P., Lohmann, K.C., and Sherrell, R.M., 2000. Incorporation and preservation of Mg in *Globigerinoides sacculifer*: implications for reconstructing the temperature and $^{18}O/^{16}O$ of seawater. Paleoceanography, 15, 135–145.

Rosenthal Y., Perron-Cashman, S., Lear, C.H., Bard, E., Barker, S., et al., 2004. Interlaboratory comparison study of Mg/Ca and Sr/Ca measurements in planktonic. Geochemistry, Geophysics, Geosystems, 5 (4), 1-29.

Rosenthal, Y., C. H. Lear, D. W. Oppo, and B. K. Linsley, 2006. Temperature and carbonate ion effects on Mg/Ca and Sr/Ca ratios in benthic foraminifera: Aragonitic species Hoeglundina elegans, Paleoceanography, 21, PA1007.

Rye, C.D., Naveira Garabato, A.C., Holland, P.R., Meredith, M.P., George Nurser, A.J., Hughes, C.W., Coward, A.C., and Webb, D.J., 2014. Rapid sea-level rise along the Antarctic margins in response to increased glacial discharge. Nature Geoscience, 7, 732–735.

Savage, M.L., Ciesielski, P.F., 1983. A revised history of glacial sedimentation in the Ross Sea region. Antarctic Earth Science, Cambridge Univ. Press, U.K., 555-559.

Scherer, R.P., Aldahan, A., Tulaczyk, S., Possnert, G., Engelhardt, H., and Kamb, B., 1998. Pleistocene collapse of the West Antarctic Ice Sheet. Science, 281, 83-85.

Scherer, R.P., Bohaty, S.M., Dunbar, R.B., Esper, O., Flores, J.-A., Gersonde, R., Harwood, D.M., Roberts, A.P., and Taviani, M., 2008. Antarctic records of precession-paced insolation-driven warming during early Pleistocene Marine Isotope State 31. Geophysical Research Letters, 35 (L03505), 1-5.

Schmidtko, S., Heywood, K.J., Thompson, A.F., and Aoki, S., 2014. Multidecadal warming of Antarctic waters. Science, 346 (6214), 1227-1231.

Schrag, D.P., 1999. Rapid analysis of high-precision Sr/Ca ratios in corals and other marine carbonates. Paleoceanography, 14 (2), 97-102.

Seidenstein, J., 2020. Plio-Pleistocene paleoceonography of the Ross Sea, Antarctica based on foraminifera from IODP Sites U1523, U1522, and U1521. Masters Theses, 937.

Shackleton, N.J., 1974. Attainment of isotopic equilibrium between ocean water and the benthonic foraminifera genus *Uvigerina*: isotopic changes in the ocean during the last glacial. Colloques Internationaux du C.N.R.S, 219, 203-208.

Shackleton, N.J., and Kennett, J.P., 1975. Paleotemperature history of the Cenozoic and the initiation of Antarctic glaciation: oxygen and carbon isotope analyses in DSDP Sites 277, 279, and 281. Initial Reports Deep Sea Drilling Project, 29, 743-755.

Shackleton, N.J., Backman, J., Zimmerman, H., Kent, D.V., Hall, M.A., et al., 1984. Oxygen isotope calibration of the onset of ice-rafting and history of glaciation in the North Atlantic region. Nature, 307, 620-623.

Shepherd, A., Wingham, D., and Rignot, E., 2004. Warm ocean is eroding West Antarctic Ice Sheet. Geophysical Research Letters, 31 (23), L23402.

Shepherd, A., Fricker, H.A., and Farrell, S.L., 2018. Trends and connections across the Antarctic cryosphere. Nature, 558, 223-232.

Shevenell, A.E., and Kennett, J.P., 2002. Antarctic Holocene climate change: A benthic foraminiferal stable isotope record from Palmer Deep. Paleoceanography, 17 (2).

Shevenell, A.E., Kennet, J.P., and Lea, D.W., 2004. Middle Miocene Southern Ocean cooling and Antarctic cryosphere expansion. Science, 305, 1766-1770.

Shevenell, A.E., Kennett, J.P., Lea, D.W., 2008. Middle Miocene ice sheet dynamics, deep-sea temperatures, and carbon cycling: a Southern Ocean perspective. Geochemistry, Geophysics, Geosystems, 9 (2), 1-14.

Shevenell, A.E., Ingalls, A.E., Domack, E.W., and Kelly, C., 2011. Holocene Southern Ocean surface temperature variability west of the Antarctic Peninsula. Nature, 470, 250-254.

Smith, L.M., Andrews, J.T., Castaneda, I.S., Kristjansdottir, G.B., Jennings, A.E., and Sveinbjornsdottir, A.E., 2005. Temperature reconstructions for SW and N Iceland waters over the last 10 cal ka based on d18O records from planktic and benthic Foraminifera. Quaternary Science Reviews, 24, 1723–1740.

Smith, W.O., Ainley, D.G., Arrigo, K.R., and Dinniman, M.S., 2014. The Oceanography and Ecology of the Ross Sea. Annual Review of Marine Science, 6, 469–487.

Smith, B., Fricker, H.A., Gardner, A.S., Medley, B., Nilsson, J., Paolo, F.S., et al., 2020. Pervasive ice sheet mass loss reflects competing ocean and atmosphere processes. Science, 368 (6496), 1239-1242.

Spero, H.J., Bijma, J., Lea, D.W., and Bemis, B.E., 1997. Effect of seawater carbonate concentration on foraminiferal carbon and oxygen isotopes. Nature, 390, 497–500.

Teitler, L., Florindo, F., Warnke, D.A., Filippelli, G.M., Kupp, G., and Taylor, B., 2015. Antarctic Ice Sheet response to a long warm interval across Marine Isotope Stage 31: A cross-latitudinal study of iceberg-rafted debris. Earth and Planetary Letters, 409, 109-119.

Theissen, K.M., Dunbar, R.B., Cooper, A.K., Mucciarone, D.A., and Hoffmann, D., 2003. The Pleistocene evolution of the East Antarctic Ice Sheet in the Prydz bay region: stable isotopic evidence from ODP Site 1167. Global and Planetary Change, 39 (3-4), 227-256.

Thoma, M., Jenkins, A., and Holland, D., 2008. Modelling Circumpolar Deep Water intrusions on the Amundsen Sea continental shelf, Antarctica. Geophysical Research Letters, 38 (L18602).

Thompson, D.W., and Solomon, S., 2002. Interpretation of Recent Southern Hemisphere Climate Change. Science, 296 (5569), 895-899.

Thompson, A.F., Stewart, A.L., Spence, P., and Heywood, K.J., 2018. The Antarctic Slope Current in a Changing Climate. Review of Geophysics, 56 (4), 741-770.

Turney, C.M., Fogwill, C.J., Golledge, N.R., McKay, N.P., van Sebille, E., et al., 2020. Early Last Interglacial ocean warming drove substantial ice mass loss from Antarctica. Proceedings of the National Academy of Sciences, 117 (8), 3996-4006.

Vázquez Riveiros, N., Govin, A., Waelbroeck, C., Mackensen, A., Michel, E., Moreira, et al., 2016. Mg/Ca thermometry in planktic foraminifera: improving paleotemperature estimations for G. bulloides and *N. pachyderma* left. Geochemistry, Geophysics Geosystems, 17, 1249-1264.

Villa, G., Persico, D., Wise, S.W., and Gadaleta, A., 2012. Calcareous nannofossil evidence for Marine Isotope Stage 31 (1 Ma) in Core AND-1B, ANDRILL McMurdo Ice Shelf Project (Antarctica). Global and Planetary Change, 96-97, 75-86.

Volkmann, R., and Mensch, M., 2001. Stable isotope composition ($\delta^{18}O$, $\delta^{13}C$) of living planktic foraminifers in the outer Laptev Sea and the Fram Strait. Marine Micropaleontology, 42 (3-4), 163-188.

Westerhold, T., Marwan, N., Drury, A.J., Liebrand, D., Agnini, C., et al., 2020. An astronomically dated record of Earth's climate and its predictability over the last 66 million years. Science, 369 (6509), 1383-1387.

Whitehead, J.M., and Bohaty, S.M., 2003. Pliocene summer sea surface temperature reconstructions using silicoflagellates from Southern Ocean ODP Site 1165. Paleoceanography, 18 (3), 1075.

Whitworth, T., and Orsi, A.H., 2006. Antarctic Bottom Water production and export by tides in the Ross Sea. Geophysical Research Letters, 33, L12609.

Wilkens, R.H., Westerhold, T., Drury, A.J., Lyle, M., Gorgas, T., and Tian, J., 2017. Revisiting the Ceara Rise, equatorial Atlantic Ocean: isotope stratigraphy of ODP Leg 154 from 0 to 5 Ma. Climate of the Past, 13, 779-793.

Williams, T., Morin, R.H., Jarrard, R.D., Jackolski, C.L., Henrys, S.A., et al., 2012. Lithostratigraphy from downhole logs in Hole AND-1B, Antarctica. Geosphere, 8 (1), 127–140.

Wilson, D.J., Bertram, R.A., Needham, E.F., van de Flierdt, T., Welsh, et al., 2018. Ice loss from the East Antarctic Ice Sheet during late Pleistocene interglacials. Nature, 561, 383-386.

Wu, G., Herguera, J.C., and Berger, W.H., 1990. Differential dissolution: modification of late Pleistocene oxygen isotope records in the western Equatorial Pacific. Paleoceanography, 5, 581–594.

Yu, J., Day, J., Greaves, M., and Elderfield, H., 2005. Determination of multiple element/calcium ratios in foraminiferal calcite by quadrupole ICP-MS. Geochemistry, Geophysics, Geosystems, 6 (8), 1-9.

Zachos, J., Pagani, M., Sloan, L., Thomas, E., Billups, K., 2001. Trends, Rhythms, and Aberrations in Global Climate 65 Ma to Present. Science, 292, 686-693.

Appendix A: Extended Data

Extended data table 1A: Elemental concentrations in standard solutions

Standard	Element (µg/mL)									
	Li	Na	Mg	Al	Ca	Sr	Ba	U	Mn	Fe
Mg/Ca 1			0.03		88					
Mg/Ca 2			0.06		88					
Mg/Ca 3			0.12		103					
Mg/Ca 4			0.19		103					
Multi-element 1	$3.1\ e^{-4}$	0.41	0.37	0.0018	100	0.34	0.0018	$6.4\ e^{-6}$	0.20	0.014
Multi-element 2	$2.2\ e^{-4}$	0.23	0.21	0.0011	103	0.31	$9.8\ e^{-4}$	$4.6\ e^{-6}$	0.013	0.013
Multi-element 3	$1.4\ e^{-4}$	0.13	0.06	$2.9\ e^{-4}$	100	0.17	$4.7\ e^{-4}$	$3.0\ e^{-6}$	0.007	0.007
Multi-element 4	$7.1\ e^{-5}$	0.08	0.01	$6.0\ e^{-5}$	104	0.10	$1.6\ e^{-4}$	$1.8\ e^{-6}$	0.003	0.003
Sample matrix	$3.1\ e^{-4}$	0.24	0.06	$4.0\ e^{-4}$	99	0.25	$8.4\ e^{-4}$	$4.5\ e^{-6}$	0.014	0.009
Multi-element 1 Parent	$6.2\ e^{-4}$	0.81	0.73	0.0036	200	0.68	0.004	$1.3\ e^{-5}$	0.040	0.027
Multi-element 1 Dilution 1	$4.7\ e^{-4}$	0.61	0.55	0.0027	151	0.51	0.003	$9.6\ e^{-6}$	0.030	0.021
Multi-element 1 Dilution 2	$9.5\ e^{-5}$	0.12	0.11	$5.5\ e^{-4}$	30	0.10	$5.6\ e^{-4}$	$1.9\ e^{-6}$	0.006	0.004
Multi-element 3 Parent	$2.8\ e^{-4}$	0.27	0.12	$5.8\ e^{-4}$	201	0.35	$9.4\ e^{-4}$	$6.1\ e^{-6}$	0.014	0.015
Multi-element 3 Dilution 1	$2.1\ e^{-4}$	0.20	0.09	$4.3\ e^{-4}$	150	0.26	$7.0\ e^{-4}$	$4.6\ e^{-6}$	0.011	0.011
Multi-element 3 Dilution 2	$4.3\ e^{-4}$	0.04	0.02	$8.7\ e^{-5}$	30	0.05	$1.4\ e^{-4}$	$9.2\ e^{-7}$	0.002	0.002
Al 1				0.005						
Al 2				0.002						
Al 3				$5.6\ e^{-5}$						

Extended data table 2A: Stratigraphic splice used for the U1523 composite depth scale (CCSF).

Hole, core, section, offset (cm)	Original depth CSF-A (m)	Rescaled depth CCSF (m)
U1523A-1H-1, 0	0.00	0.00
U1523A-1H-5, 14	6.15	6.15
U1523E-1H-5, 9	6.09	6.15
U1523E-1H-7, 27	9.28	9.34
U1523A-2H-1, 103	9.53	9.34
U1523A-2H-CC, 17	16.01	15.82
U1523E-3H-1, 0	16.00	16.54
U1523E-3H-3, 96	19.97	20.51
U1523A-3H-2, 64	19.97	20.51
U1523A-3H-CC, 20	25.20	25.73
U1523A-4F-1, 0	27.50	28.03
U1523A-4F-CC, 33	30.98	31.51
U1523A-5F-1, 0	32.20	32.73
U1523A-5F-2, 34	33.32	33.85
U1523E-7F-1, 0	34.70	34.82
U1523E-7F-CC, 8	35.18	35.30
U1523A-6F-1, 0	36.90	37.43
U1523A-6F-CC, 17	41.64	42.17
U1523A-7F-1, 0	41.60	42.36
U1523A-7F-CC, 12	42.55	43.34
U1523B-3F-1, 0	46.70	47.72
U1523B-3F-CC, 6	49.50	50.52
U1523B-5F-1, 0	56.10	57.12
U1523B-5F-CC, 14	60.37	61.39
U1523E-12F-1, 0	60.00	61.62
U1523E-12F-CC, 18	64.85	66.47
U1523B-7F-1, 0	65.50	66.52
U1523B-7F-CC, 43	70.30	71.32
U1523B-8F-1, 0	70.20	71.72
U1523B-8F-CC, 30	74.76	76.28
U1523B-9F-1, 0	74.90	76.42
U1523B-9F-CC, 19	76.19	77.71
U1523B-10F-1, 0	79.60	81.12
U1523B-10F-4, 34	83.69	85.21
U1523E-15F-1, 38	82.08	85.21
U1523E-15F-CC, 7	86.13	89.26
U1523E-16F-1, 0	86.40	89.53
U1523E-16F-CC, 23	90.82	93.95

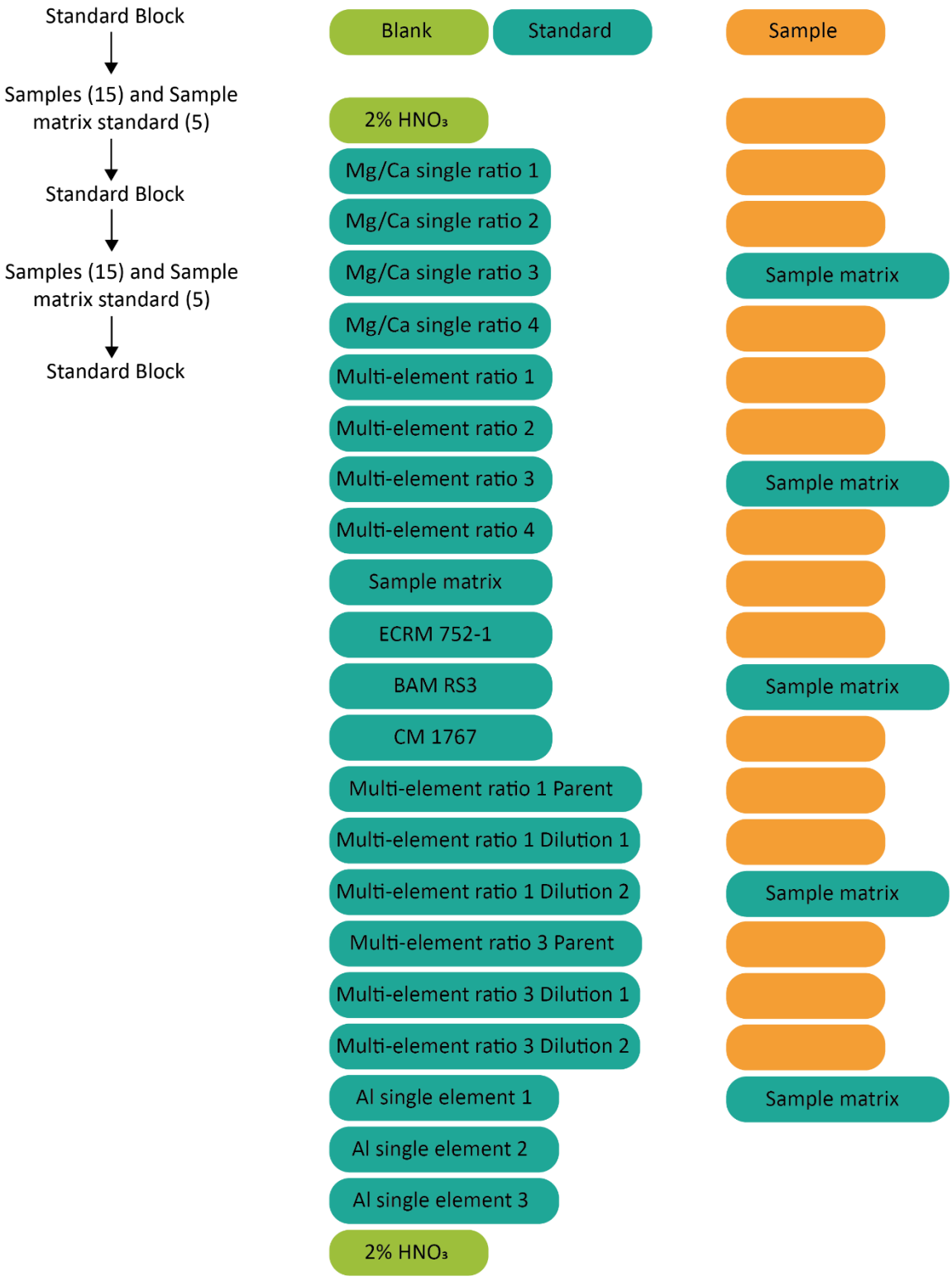

Extended data figure 1A: Typical XR ICP-MS sequence for trace element/Ca analysis.

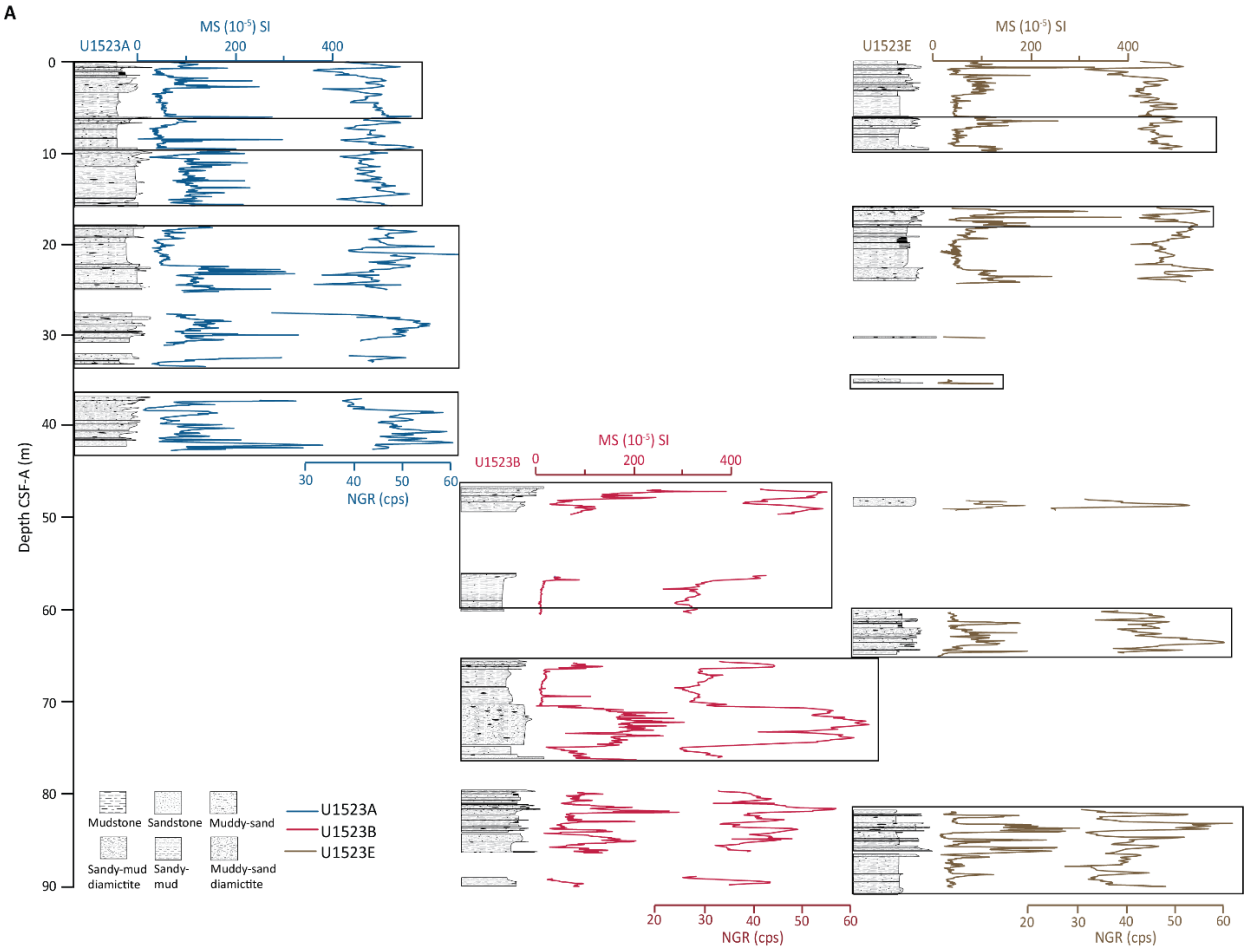
A
U1523A
MS (10-5) SI
0
200
400
U1523E
MS (10-5) SI
0
200
400
U1523B
MS (10-5) SI
0
200
400
Depth CSF-A (m)
0
10
20
30
40
50
60
70
80
90
30
40
50
60
NGR (cps)
20
30
40
50
60
NGR (cps)
20
30
40
50
60
NGR (cps)
Mudstone
Sandstone
Muddy-sand
Sandy-mud diamictite
Sandy-mud
Muddy-sand diamictite
U1523A
U1523B
U1523E

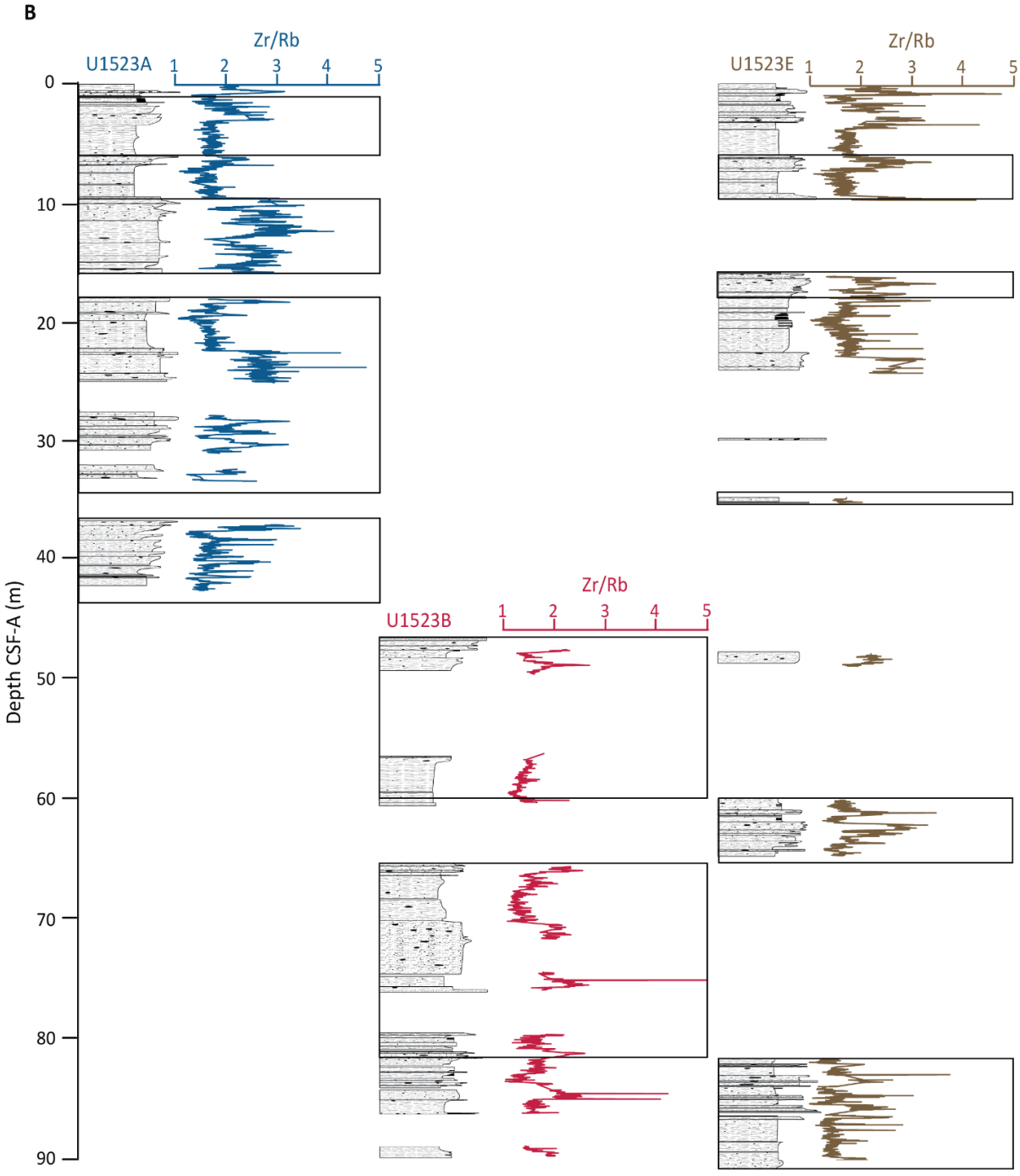

Extended data figure 2A: U1523 detailed lithology, physical properties, and XRF-Zr/Rb records used to generate the splice. The splice was generated by correlating lithology, (A) MS and NGR, and (B) Zr/Rb against the shipboard CSF-A scale across the three holes cored at U1523. Black boxes surround the intervals incorporated into the splice from Holes U1523A

(blue), B (red), and E (brown) (Extended data table 2). Zr/Rb is expressed as X-ray fluorescence (XRF) scan counts.

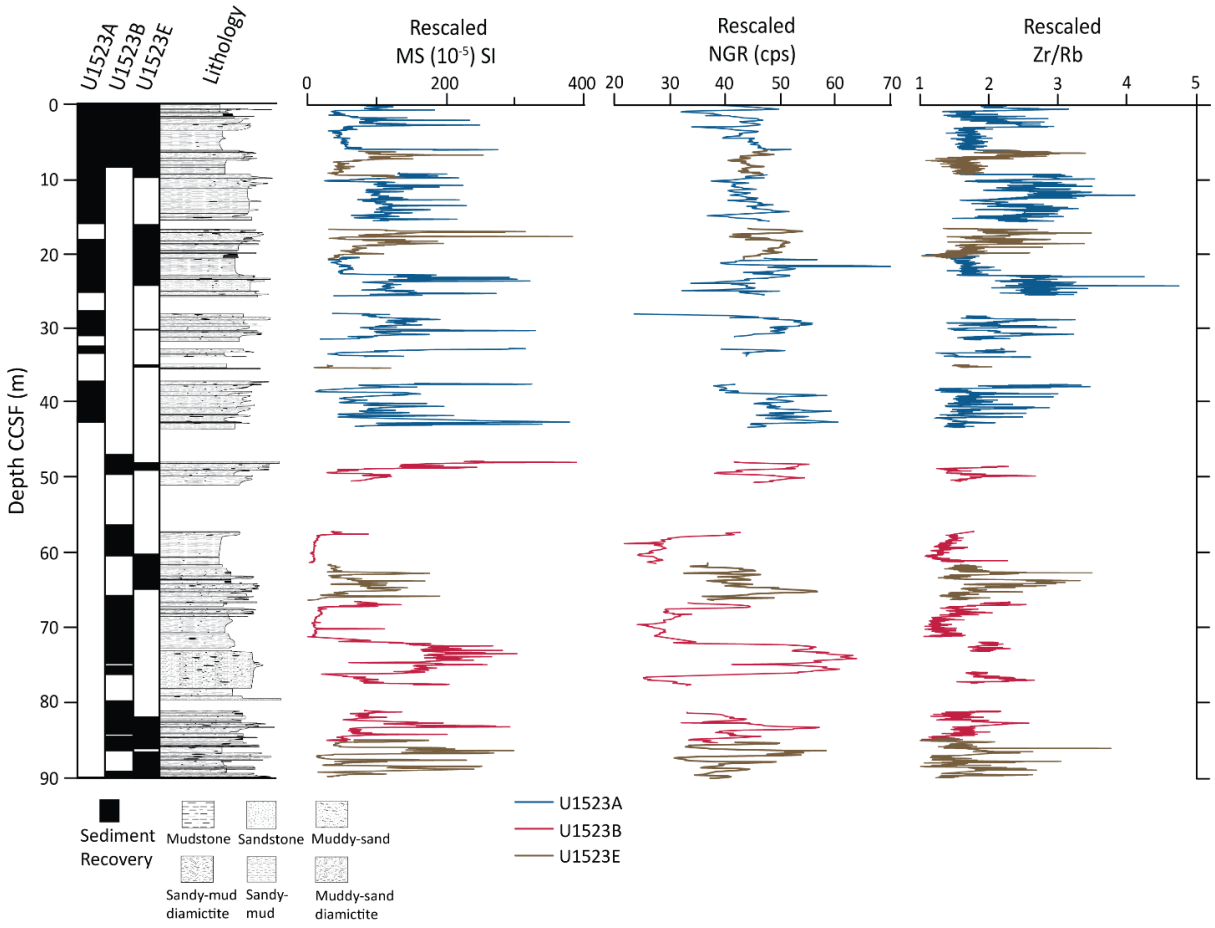

Extended data figure 3A: Rescaled physical properties and Zr/Rb against the composite depth below sea floor (CCSF) scale. Sediment recovery is shown as black bars in the three holes cored at Site U1523.

Appendix B: Permissions

Copyright information for Figure 1 from "Four decades of Antarctic Ice Sheet mass balance from 1979–2017," by Rignot et al. (2019), Proceedings of the National Academy of Sciences, 116 (4), 1095–1103.

Article Information

vol. 116 no. 4 1095-1103

DOI: https://doi.org/10.1073/pnas.1812883116
PubMed: 30642972

Published By: National Academy of Sciences
Print ISSN: 0027-8424
Online ISSN: 1091-6490
History: Published in issue January 22, 2019.
Published first January 14, 2019.

Article Versions

- Previous version (January 14, 2019 - 11:47).
- You are viewing the most recent version of this article.

Copyright information for Figure 2 modified from “An astronomically dated record of Earth's climate and its predictability over the last 66 million years” by Westerhold et al. (2020). Science, 369 (6509), 1383-1387.

Science AAAS

License to Publish

The following Grant of License ("License") must be signed and returned to the American Association for the Advancement of Science ("AAAS") before a manuscript can be accepted for publication. If the copyright in the contribution is owned by the author's employer, the employer or an authorized representative must sign this form. In the event that AAAS decides not to publish the Work, this License shall be null and void.

1. In consideration of publication by AAAS in one of its *Science* journals of the work currently titled _____ and all associated supplemental materials, data, audio and/or video files (the "Work") and authored by _____ ("Author"), the sole and exclusive, irrevocable right is hereby granted to AAAS to publish, reproduce, distribute, transmit, display, store, translate, create derivative works from and otherwise use the Work in any form, manner, format, or medium, whether now known or hereafter developed, throughout the world and in any language, for the entire duration of any such right and any renewal or extension thereof and to permit/sublicense others to do any or all of the foregoing as well.

2. Ownership of the copyright shall remain with the Author, subject to the rights granted to AAAS in paragraph 1. AAAS shall be the holder of title for purpose of registration.

3. Author also retains the non-exclusive right to use the Work in the following ways without further permission but only after publication of the Work by AAAS and subject to the requirement that credit be given to its first publication in the appropriate issue of the applicable *Science* journal: **1)** Reprint the Work in print collections of Author's own writings; **2)** Reprint the Work in print format for inclusion in a thesis or dissertation that the Author writes; **3)** Present the Work orally; **4)** Reproduce the Work for use in courses the Author is teaching (If the Author is employed by an academic institution, that institution may also reproduce the Work for course teaching); **5)** Distribute photocopies or a PDF of the Work to colleagues for non-commercial purposes only (providing that recipients are informed that they may not further distribute or copy the Work); **6)** Post a copy of the "Accepted Version" of the Work (the version of the paper accepted for publication by AAAS including changes resulting from peer review but prior to AAAS's copy editing and production) on the Author's personal website or in his/her Institution's archival database repository, provided a hyperlink to the Work on the *Science* website is included and provided the "Accepted Version" is marked with the following notice: "This is the author's version of the work. It is posted here by permission of the AAAS for personal use, not for redistribution. The definitive version was published in *Science* Journal Title {VOL#, (DATE)}, doi: {doi number for your manuscript}"; **7)** Reuse figures and tables created by the Author in future works the Author writes; **8)** The Author's employer may use the "Accepted Version" of the Work for non-commercial research purposes ("Non-commercial research purposes" is defined as research undertaken for purposes other than (a) a profit motive, (b) for commercial exploitation, (c) monetary gain derived from the outcome of the research, (d) research undertaken on behalf of a commercial entity, or (e) other similar purposes); **9)** Author may use or authorize use of Supporting Online Material associated with the Work for any purpose and in any format.

4. In addition to the rights retained by the Author in 3 above, authors of research articles, reports, brevia, reviews, or technical comments arising out of grants awarded no earlier than 2 May 2005 who are required by their funding agencies to make their research results publicly available may do so under the following conditions: The Author may cause the posting, no sooner than 6 months after final publication of the Work by AAAS, of the "Accepted Version" of the Work in his/her funding body's archive or designated repository provided it includes a hyperlink to the final published version on the *Science* website and the full reference citation and provided that further use of the posted article copy is restricted to non-commercial research purposes ("Non-commercial research purposes" is defined as research undertaken for purposes other than (a) a profit motive, (b) for commercial exploitation, (c) monetary gain derived from the outcome of the research, (d) research undertaken on behalf of a commercial entity, or (e) other similar purposes). The "Accepted Version" shall be defined as the version of the paper accepted for publication by AAAS including changes resulting from peer review but prior to AAAS's copy editing and production. This policy does not apply to article types that are not specifically mentioned above. The Author must ensure that the "Accepted Version" is not released on his/her funding body's archive or repository until 6 months after its final publication date in a *Science* journal.

5. In order that we may preserve the commercial value of our publication, Author agrees to obtain authorization from AAAS in advance for any uses not expressly described in paragraphs 3 or 4.

6. Author warrants and represents that the Work is original, that all the facts contained therein are true and accurate, and that the Work has not been published elsewhere, and does not infringe upon any copyright, proprietary, or personal right of any third party. If the Work contains any material that is owned or controlled by a third party, Author certifies that he/she has obtained permission for its use (please attach evidence of this) and that the material is clearly acknowledged within the text.

7. Author further warrants and represents that to the extent that Author's right and ability to grant to AAAS all rights specified in Paragraph 1 above is or might be limited by a university policy or other institutional restrictions, Author has obtained a waiver of such policy or restrictions from the applicable university or institution.

By signing this agreement, Author warrants that he/she has the full power to enter into this agreement. This agreement shall remain in effect throughout the term of copyright in the Work and may not be revoked without the express written consent of both parties.

This Agreement shall be governed and construed, and any dispute arising hereunder resolved, in accordance with the laws of the District of Columbia, United States of America, without resort to the conflicts of laws principles thereof.

_____

Author's Name (please print)

_____

Author's Signature

For Authors employed by the United States Government: I attest that the above article was written as part of my official duties as an employee of the U.S. Government (and therefore the article is in the public domain).

_____

Author's Name (please print)

_____

Author's Signature

For works created under U.S. Government Contract: Please sign the top portion of this agreement. The AAAS recognizes the U.S. Government's non-exclusive rights to use the Work for non-commercial, governmental purposes where such rights are established in the grant or contract.
Works subject to Crown Copyright: For authors employed by the Australian, Canadian, and/or UK Governments, please contact AAAS for an alternate form.

Copyright information for Figure 3 Modified from McKay, R.M., De Santis, L., Kulhanek, D.K., and the Expedition 374 Scientists, 2019. Ross Sea West Antarctic Ice Sheet History. Proceedings of the International Ocean Discovery Program, 374: College Station, TX (International Ocean Discovery Program).

ISSN

World Wide Web: 2377-3189

Volume DOI

https://doi.org/10.14379/iodp.proc.374.2019

Publication date

10 August 2019